AUTHOR ACCEPTED MANUSCRIPT Cerfontaine, Benjamin et al. "A Finite Element approach for determining the full load-displacement relationship of axially-loaded shallow screw anchors, incorporating installation effects". Canadian Geotechnical Journal. June 2020. DOI 10.1139/cgj-2019-0548

Title

A Finite Element approach for determining the full load-displacement relationship of axially-loaded shallow screw anchors, incorporating installation effects

Author list

Benjamin Cerfontaine*, Jonathan A. Knappett, Michael J. Brown, Craig S. Davidson, Therar Al-Baghdadi, Yaseen U. Sharif, Andrew Brennan, Charles Augarde, William M. Coombs, Lei Wang, Anthony Blake, David J. Richards and Jon Ball

**Corresponding author*

Author details

Benjamin Cerfontaine, BSc, MSc, PhD

MSCA Research Fellow, School of Science and Engineering, University of Dundee, Fulton Building, Dundee, DD1 4HN, UK

ORCID: 0000-0002-4833-9412

Email: b.cerfontaine@dundee.ac.uk

Jonathan A. Knappett, MA MEng PhD GMICE

Professor, School of Science and Engineering, University of Dundee, Fulton Building, Dundee, DD1 4HN, UK

ORCID: 0000-0003-1936-881X

Email: j.a.knappett@dundee.ac.uk

Michael J. Brown, BEng PhD GMICE

Reader, School of Science and Engineering, University of Dundee, Fulton Building, Dundee, DD1 4HN, UK

ORCID: 0000-0001-6770-4836

Email: m.j.z.brown@dundee.ac.uk

Craig Davidson, BSc MSc

Research Associate, School of Science and Engineering, University of Dundee, Fulton Building, Dundee, DD1 4HN, UK

ORCID: 0000-0002-4843-5498

Email: c.s.davidson@dundee.ac.uk

Therar Al-Baghdadi, BSc, MSc, PhD

Geotechnical Engineer, Municipality of Karbala, Karbala, Iraq

ORCID: 0000-0002-7368-4285

Email: therarb@yahoo.co.uk

Yaseen U Sharif, BSc, MSc

PhD student, School of Science and Engineering, University of Dundee, Fulton Building, Dundee, DD1 4HN, UK

ORCID: 0000-0002-3620-7500

Email: y.u.sharif@dundee.ac.uk

Andrew J. Brennan, MEng PhD GMICE

Senior Lecturer, School of Science and Engineering, University of Dundee, Fulton Building, Dundee, DD1 4HN, UK

ORCID: 0000-0002-8322-0126

Email: a.j.brennan@dundee.ac.uk

Charles Augarde, BSc MSc DPhil CEng FICE

Professor, Department of Engineering, Durham University, Durham, DH1 3LE, UK

ORCID: 0000-0002-5576-7853

Email: charles.augarde@durham.ac.uk

Will M. Coombs, MEng PhD

Associate Professor, Department of Engineering, Durham University, Durham, DH1 3LE, UK

ORCID: 0000-0003-2099-1676

Email: w.m.coombs@durham.ac.uk

Lei Wang, PhD

Research Assistant, Department of Engineering, Durham University, Durham, DH1 3LE, UK

Email: lei.wang@durham.ac.uk

Anthony Blake, BEng, PhD

Research Fellow, Faculty of Engineering and the Environment, University of Southampton, SO17 1BJ, UK

ORCID: 0000-0001-5718-7900

Email: a.p.blake@soton.ac.uk

David J. Richards, BEng MSc PhD CEng MICE

Professor, Faculty of Engineering and the Environment, University of Southampton, UK

ORCID: 0000-0002-3819-7297

Email: djr@soton.ac.uk

Jon Ball, EurGeol Bsc. (Hons) CGeol FGS

Chief Geotehcnical Engineer, Roger Bullivant Ltd, Swadlincote, UK

Email: Jon.Ball@roger-bullivant.co.uk

Main text word count: 7602

Number of tables: 6

Number of Figures: 16

A Finite Element approach for determining the full load-displacement relationship of axially-loaded shallow screw anchors, incorporating installation effects

B. Cerfontaine*, Jonathan A. Knappett, Michael J. Brown, Craig S. Davidson, Therar Al-Baghdadi, Andrew J. Brennan, Charles Augarde, William M. Coombs, Lei Wang, Anthony Blake, David J. Richards and Jon Ball

ABSTRACT

Screw anchors have been recognised as an innovative solution to support offshore jacket structures and floating systems, due to their low noise installation and potential enhanced uplift capacity. Results published in the literature have shown that for both fixed and floating applications, the tension capacity is critical for design but may be poorly predicted by current empirical design approaches. These methods also do not capture the load-displacement behaviour, which is critical for quantifying performance under working loads. In this paper, a Finite Element methodology has been developed to predict the full tensile load-displacement response of shallow screw anchors installed in sand for practical use, incorporating the effects of a pitch-matched installation. The methodology is based on a two-step process. An initial simulation, based on wished-in-place conditions, enables the identification of the failure mechanism as well as the shear strain distribution at failure. A second simulation refines the anchor capacity using soil-soil interface finite elements along the failure surface previously identified and also models installation through successive loading/unloading of the screw anchor at different embedment depths. The methodology is

validated against previously published centrifuge test results. A simplified numerical approach has been derived to approximate the results in a single step.

KEYWORDS

Screw anchor, Helical Pile, Sand, Finite element modelling, Design

INTRODUCTION

Screw anchors or piles are a foundation technology that may provide significant uplift capacity for offshore applications (Byrne and Houlsby 2015; Houlsby 2016) while avoiding pile driving nuisance for marine inhabitants (Bailey et al. 2010). Screw anchors consist of one or more steel helices (150-400mm diameter), attached to a core of smaller diameter and are used onshore to anchor relatively light structures (Perko 2009). These anchors are screwed into the soil by applying a torque and a crowd force to ensure penetration with a minimum soil disturbance (Perko 2009). Such anchors, if appropriately scaled-up, may be suitable to provide the very large tension requirements of bottom-fixed jacket structures (e.g. 20MN, (Byrne and Houlsby 2015)) or floating tension-leg platforms (e.g. 10MN, (Bachynski and Moan 2014)) for offshore wind turbines.

The uplift capacity of shallow screw anchors was investigated by Davidson et al. (2019) through centrifuge testing in medium-dense and dense sand. The centrifuge uplift capacities were compared with results published in the literature, as shown in Figure 1. This figure presents a non-dimensional bearing factor, N_γ, obtained by normalising the uplift capacity with respect to the helix embedment depth H, the area of the helix and the buoyant unit weight γ',

$$N_\gamma = \frac{F_y}{\gamma' HA}. \quad (0)$$

Centrifuge results are consistent with the other experimental results, as shown in Figure 1. Bearing factors obtained by Ilamparuthi et al. (2002) constitute the upper bound of the results presented, especially at larger relative embedment. This is probably due to their relatively small scale, being tested at 1g, leading to a more pronounced effect of dilatancy on the soil response. Conversely, centrifuge tests provide a lower bound. Centrifuge results of Dickin (1988) were reported for comparison, but were related to square plate anchors, which have been shown to provide lower uplift capacity (Giampa et al. 2018a).

Byrne and Houlsby (2015) stated that multi-footing structures such as tripods or jacket structures will become necessary to deploy wind turbines in deeper water. In this case, the tensile capacity is the critical design case and screw anchors can provide sufficient capacity. However typical analytical approaches (e.g. Mitsch and Clemence 1985) may significantly overpredict the screw anchor capacity for these large scale applications. The recent semi-analytical method proposed by Giampa *et al*. (2017) for shallow anchors which is based on peak friction and dilatancy angles for shallow anchors, assumes that the failure mechanism can be described by a shallow wedge, whose inclination to the vertical direction is equal to the dilatancy angle. This finding is similar to the work of White et al. (2008) for the uplift of buried pipelines and has been theoretically justified for anchors by Vermeer and Sutjiadi (1985). However, the method is limited to single helix screw anchors and does not provide any load-displacement (stiffness) information, which is very important for jacket structures and tension-leg platforms, as the axial stiffness controls the global rotational stiffness of the wind turbines. For instance, the rotation of bottom-fixed wind turbines must typically be kept below 0.5° to ensure safe operation (Achmus *et al*. 2009).

Finite Element modelling enables the prediction of the entire tensile load-displacement relationship, but few studies have previously tackled this problem for screw anchors in cohesionless soils due to the difficulties in capturing the effects of installation (a large displacement process) on capacity. Those approaches which have been proposed for modelling the problem rely on back-calculated parameters, characterising the soil properties around the anchor, to reproduce field or experimental tests (e.g. Papadopoulou et al. 2014; Mosquera et al. 2015; Perez et al. 2018) without which uplift capacities are overestimated (e.g. Gavin et al. 2014) due to an incorrect modelling of the strength mobilised at failure. On the other hand, the installation process is a large deformation process which strongly modifies the void ratio (e.g. tomography results presented in Schiavon (2016)) and stress state around the anchor, modifying the stiffness of the anchor. Giampa et al. (2017) used limit analysis and finite element methods to simulate small-scale 1g tests. However, they focused on anchor capacity and did not provide any comparison of the load-displacement behaviour or initial stiffness. Consequently, there is a need to develop a new methodology to better predict both the uplift capacity and initial stiffness that does not rely physical testing for deriving global empirical parameters and which is simple enough to be used in the practical design of screw anchors.

The objective of this study is to define a flexible methodology to predict drained tensile performance of shallow screw anchors representative of offshore applications (full load-displacement behaviour, incorporating capacity and stiffness) using the Finite Element method in 2D axisymmetric conditions, which accounts for the effects of a drained installation process in a simplified way. This method is based on a well-defined numerical

procedure requiring measurable, rather than arbitrarily defined soil parameters and is applicable to a range of geometries (helix number and spacing). This will address the key limitations of existing analytical and numerical capacity models and will provide a method for determining both stiffness (as necessary to calculate natural frequencies of a foundation-renewable device system) and capacity (i.e. a virtual load test) for informing practical design. Single and double large helix diameter screw anchor centrifuge load tests, published by (Davidson et al. 2020) and wished-in-place typical onshore screw anchors Hao et al. (2018), will be used to validate the finite element analyses. The shape of the failure mechanism, the stress and strain distributions along the failure mechanism are key variables that are studied in detail in order to develop a reliable method for design.

PHYSICAL AND NUMERICAL MODELS

The Finite Element (FE) method cannot be used to reproduce the exact large-deformation installation process, with other methods being preferable (Wang et al. 2017). However, the FE method offers a good compromise between the simulation cost and accuracy of results. The objective of this work is to develop a modelling approach that is practically applicable in the design screw anchors for offshore applications. Consequently, it must be achievable within commercial software (e.g. PLAXIS software (PLAXIS 2017a)), it must be fast (2D axisymmetric analysis) and it must be based on typical constitutive models (e.g. the Hardening soil model (Schanz et al. 1999a)) relying on a limited number of measurable parameters that can be determined using routine laboratory ad in-situ test methods. The numerical modelling methodology as well as physical (centrifuge) models used to validate it are described in this section.

120 ***Centrifuge tests***

121 Numerical results are validated against two sets of small-scale centrifuge tests undertaken at
122 the University of Dundee (UoD) (Davidson et al. 2019) and the University of Western
123 Australia (UWA) (Hao et al. 2018), both in dense sand. Prototype geometries and important
124 variables are summarised in Table 1, along with tensile capacity F_y.

125

126 The tests undertaken at the University of Dundee, extensively described in (Davidson et al.
127 2019) incorporate the installation effect. Three screw anchors were installed in a very dense
128 sand (referred to as VD, D_r = 84% on average) and one in a medium dense sand (MD, D_r =
129 57%). The tests were undertaken in dry sand at 48g. The stress field generated within the
130 sand box was identical to the effective stress field that would be obtained in a saturated
131 sand at 80g – an approach explained and justified in Li et al. (2010). This approach has
132 previously been validated for lateral pile loading by Klinkvort et al. (2013). The helix
133 diameter D_h of all model anchors installed in very dense sand was equal to 1.7m at prototype
134 scale (scaling factor equal to 80g). Two of these models (U1VD-A and U1VD-B) had a single
135 helix while the third one (U2VD) possessed two helices whose spacing was equal to 2 helix
136 diameters. The helix diameter of the model (U1MD) installed in medium-dense sand was
137 equal to 3.4m. The core diameter D_c was equal to 0.88m for very dense sand models and
138 1.13m for the medium-dense sand. The helix pitch was constant and equal to 0.56m. All
139 models were installed at a constant rotation rate equal to 3RPM. The advancement rate was
140 chosen to equal one helix pitch per revolution to limit disturbance, i.e. pitch-matched
141 installation as recommended in the literature (Perko 2000). The vertical load or crowd force
142 ($F_{y,min}$) required to maintain the prescribed penetration rate of the model was recorded
143 during the test. The installation process and the uplift loading in both centrifuge tests and

144 numerical simulations were imposed sufficiently slow to represent drained installation and
145 loading conditions, representative of the offshore conditions. The tests were also modelled
146 dry to assure this was the case as mentioned previously.
147
148 The second set of data used for independent validation consists of tests published by Hao et
149 al. (2018). These tests consist of flat plate and helical plate anchors (0.4m diameter) were
150 placed into a strongbox and the sand was pluviated all around them, before each anchor was
151 tested in tension. In this case, there is no installation effect and the model anchors can be
152 considered as experimentally wished-in-place. The target global density of the different
153 samples ranged between 85% and 96% and the samples were spun at 20g. The helix
154 diameter D_h at the prototype scale was equal to 0.4m while the core diameter D_c was equal
155 to 0.094m. The helix pitch was constant and equal to 0.1m at prototype scale.
156
157 General scaling laws and practical recommendations were respected to ensure the similitude
158 of centrifuge tests at prototype scale (Garnier et al. 2007). The diameter of the smallest
159 helix/plate (D_h) to the mean grain size (d_{50}) considered here exceeds 150. If it is assumed that
160 helix behaviour is controlled by shear band propagation, this value must exceed the range of
161 50 to 100 recommended in Garnier et al. (2007). Additionally, this also exceeds the
162 recommendations in for grain size effects on pull out of anchors reported by Garnier et al.
163 (2007) of plate width, B ratio to d_{50} of greater than 48. In addition, the helix pitch to d_{50} ratio
164 was larger than 50, which was assumed adequate to allow the movement of all particles
165 throughout the helix during the installation process. Studies based upon Discrete Element
166 modelling (DEM) with far fewer particles actually modelled between the helix plates showed
167 good correlations with centrifuge testing (Sharif et al. 2019). The smallest pile shaft diameter

gave a minimum value of $79d_{50}$ satisfying the lower bound recommendation in Garnier et al. (2007) of 50 times d_{50} regarding the ratio of pile to average grain size diameter.

Geometry of the numerical model

In terms of screw pile geometry it is common to idealise the helices as horizontal plates connected to the pile core at a depth representative of the mid pitch of the true helix (Livneh and El Naggar 2008; Al-Baghdadi 2018; Pérez et al. 2018). This hypothesis has been tested through centrifuge experiments on wished-in-place (WIP) screw anchors by Hao et al. (2018), who showed that the uplift capacity of flat and helical plates was almost identical. A similar result was found numerically for WIP anchors by (Al-Baghdadi 2018). This simplification allows screw anchors to be modelled under axisymmetric conditions due to the symmetry of the geometry and loading (in tension or compression). The anchor elements were here modelled using 5-node plate elements based on Reissner-Mindlin's theory (Zienkiewicz and Taylor 2000). The properties of the plates, matching the centrifuge models, are reported in Table 2. The anchor and helix structural behaviour was assumed to be purely elastic. Elastic structural response was observed for all centrifuge test cases considered and would be desirable in design. The thickness of the plate and helix used at UWA was not specified, therefore they were assumed very stiff and the same helix/plate properties were used for all tests.

The soil was modelled by 15-node triangular 2D axisymmetric elements. The mesh was chosen to be a good compromise between accuracy of results and CPU time required for simulations. It was different for each geometry, but all meshes were refined close to the helices and in a zone extending to $3.5D_h$ from the anchor core so that failure surface could be modelled with enough precision. The boundary conditions were representative of the centrifuge tests in each case and were sufficiently spaced from the screw anchors to avoid any interference. The bottom boundary lies $7D_h/10D_h$ below the helix while the lateral

boundary was located $17D_h/30D_h$ from the core for UoD and UWA tests respectively. The displacement was fully fixed along the bottom boundary and normally fixed (i.e. allowing vertical displacement) along the vertical boundaries. The numbers of elements used for each screw anchor mesh are reported in Table 3. A force (for load-controlled stages during installation modelling) or displacement (for displacement-controlled virtual load test) was applied at the top of the shaft to be consistent with the centrifuge experiments.

Zero-thickness 5-node interface elements were used to simulate the interactions between the helix/core and the soil or shear bands within the soil (see later). They were defined on each side of the plate elements. These interface elements allow the opening of a gap between plate and soil when the contact stresses reduce to zero, as well as tangential sliding after friction mobilisation.

Soil constitutive model

The 'hardening soil model with small strain stiffness' (HSsmall) was adopted to simulate the sand behaviour (Schanz 1998; Schanz et al. 1999b; PLAXIS 2017b). The parameters of the HST95 Congleton sand, used for the centrifuge tests at the UoD, have been calibrated previously against laboratory element tests as described elsewhere (Lauder et al. 2013; Al-Defae et al. 2013). The use of this model has been comprehensively validated against 1-g, centrifuge and field tests, encompassing various boundary value problems, including piles (e.g. Al-Defae *et al.* 2013; Knappett *et al.* 2016; Al-Baghdadi *et al.* 2017).

The constitutive model is composed of a shear-strain hardening yield surface. It assumes that the stress and strain describe a hyperbolic relationship for the primary triaxial loading of

a soil sample and the yield surface converges towards the Mohr-Coulomb surface. It encompasses a tension cut-off to prevent tension loading of the soil and a second volumetric strain hardening yield surface to reproduce oedometric stress paths. The model stiffness is confinement dependent and secant stiffness degrades as shear strain increases. The unloading/reloading elastic stiffness is not a function of the shear strain. The volumetric behaviour is non-associated and is related to the dilatancy angle as reported elsewhere (PLAXIS 2017b). It includes a dilatancy cut-off, ensuring the current void ratio remains lower or equal to the maximum void ratio. All parameters used for the very-dense and medium-dense models are reported in Table 4. They were previously determined for a large range of relative densities based on shearbox and oedometer tests by Al-Defae *et al.* (2013) and were subsequently further validated against drained triaxial compression tests.

The UWA samples were prepared in a dry fine to medium sub-angular silica sand, at relative densities ranging from 85% to 96%. There is no published triaxial data to calibrate the HSsmall model parameters, only the critical state friction angle $\phi'_{cv}(¿31°)$ was provided in the paper and the authors assumed that the peak friction angle ϕ'_{pk} could be calculated according to

$$\phi'_{pk} = \phi'_{cv} + m_{tr} I_R \quad (0)$$

where I_R is the relative dilatancy angle and $m_{tr} = 3$ for triaxial conditions are obtained from (Bolton 1986).

$$I_R = 5D_r - 1. \quad (0)$$

The resulting peak friction angles range from 41.2° to 42.4° respectively. The dilatancy angle was selected to be consistent with the formulation of the hardening soil model (Schanz and Vermeer 1996)

$$\sin\psi'_{pk} = \frac{\sin\phi'_{pk} - \sin\phi'_{cv}}{1 - \sin\phi'_{pk}\sin\phi'_{cv}} \quad (0)$$

for which the dilatancy index ranges from 12.3° to 14.1°. The buoyant unit weight varies between 10.5 and 10.6kN/m^3. The rest of the parameters, especially stiffness parameters, are assumed to be identical to the HST95 sand parameters and are defined as a function of the relative density in Table 4.

The interface behaviour was also described by the HSsmall model. For the soil-steel interface elements, the friction and dilatancy angle were defined equal to 27° and 0° respectively, (Lauder et al. 2013). The dilatancy angle of the soil-soil interface at the critical state was set equal to zero while it remained equal to the peak value otherwise. The soil was assumed completely saturated (with a fully drained response) and the water level was located at the soil surface.

Modelling methodology

The methodology developed to capture both a consistent anchor capacity and stiffness is described here and summarised in Figure 2. The methodology is based on two successive numerical simulations of increasing complexity (stages 1 and 2), with output from the first stage informing the second. This multi-stage approach allows for the effects of installation-induced soil stress distribution disturbance to be modelled in a self-contained and approximate way, without requiring centrifuge or field load test data to back-calculate appropriate soil parameters in disturbed soil, and is therefore a significant improvement for practical application compared to the recent method of Perez et al. (2018). It is based only on known geometrical parameters of the screw anchor, the in-situ relative density, which in sands can be used to determine the required soil parameters (Table 4), and the measured crowd force during installation. This final parameter can be predicted using the CPT-based

relationships presented by Davidson et al. (2018), and can subsequently be refined using measurements from the installation rig in the field or on the centrifuge. However, this procedure does not reproduce the soil displacement due to the shaft penetration and helix movement. The extrapolation of the results to geometries inducing significantly larger or lower shaft diameters should then be done cautiously.

The stage 1 simulations (Figure 2(a)) were based on the minimal number of hypotheses and composed of three distinct phases. Firstly, the geostatic stress field distribution was initialised within the soil. The initial distribution of the horizontal stresses was based on the Jaky formula (Jaky 1944) and the screw anchor is considered to be wished-in-place at a depth corresponding to each test. Secondly, the compression load corresponding to the recorded installation crowd force at the final helix depth was applied under load control, then reduced to zero (simulating removal of the installation rig). Finally, a vertical upward displacement was imposed at the top of the core to simulate the uplift. The numerical simulations were stopped when the ultimate capacity was reached which corresponds to vertical displacements ranging from 0.1 to $0.3D_h$. Failure of the anchor corresponds to a peak or plateau in the load-displacement relationship and the formation of an uplift failure mechanism, as reported in Figure 2(a).

In stage 2, the numerical model was enhanced to improve the prediction of both anchor capacity and initial stiffness. To improve the capacity prediction (Figure 2(b)), discrete soil-soil interface elements, oriented along the shear plane locations identified from stage 1, were introduced in the mesh, as shown in Figure 2(b). Reduced strength parameters, corresponding to localised soil softening, were defined over a limited zone, based on the

286 analysis of the magnitudes of the shear strains, as shown in Figure 2(b). This analysis is made
287 by inspection of shear strain contour plots at failure (peak or plateau in the load-
288 displacement relationship) from stage 1 simulations. It can be assumed that the soil will
289 enter the post-peak softening regime for shear strain larger than a given threshold. This
290 variable can be obtained from experiments, e.g. as the strain at which critical state strength
291 is achieved from a direct shear test. For the HST95 sand, it is approximately 7.5% as in (Al-
292 Defae et al. 2013), or approximately 15% from triaxial tests (Robinson 2016). For the cases
293 presented herein, this threshold strain was assumed equal to be 10% for the HST95 sand
294 used by Davidson et al. (2019) and it was assumed identical for application to the results of
295 (Hao et al. 2018) as no specific element test results for this case were available. The distance
296 over which a shear strength corresponding to the critical state parameter can then be
297 identified by inspection of the shear strain contour in the FE software. The corresponding
298 interface properties are then assigned to two different zones, corresponding to the softening
299 and peak states.
300 This approach can be defined as a hybrid FE-Limit Analysis and has several advantages for
301 practical design. It incorporates the effect of soil volumetric compression on the failure
302 mechanism, unlike Limit Analysis (as reported in Cerfontaine et al. 2019). In addition, the
303 approach does not require complex numerical solutions to avoid problems resulting from
304 the use of strain-softening models (Anastasopoulos et al. 2007). Indeed, real shear bands
305 have the width of several sand grains (5 to $40d_{50}$, where d_{50} is mean particle size of the sand
306 (Desrues and Viggiani 2004; Lauder et al. 2012)), which reduces almost to a zero-thickness
307 interface at the scale of a boundary value problem. The rigorous simulation of such shear
308 bands would require an extremely fine mesh (size equal to approximatively $3d_{50}$; Gudehus

309 and Nübel 2004) or regularisation techniques introducing some mesh-size dependence, (e.g.
310 Anastasopoulos et al. 2007).
311 Also, in stage 2 (Figure 2(c)), the stiffness prediction was improved by considering the stress
312 field modification around the anchor due to the varying crowd force applied during its
313 installation. Indeed, this force induces settlement and generates soil hardening over a zone
314 which is several helix diameters wide around the anchor. This installation effect is
315 approximated by simulating several loading/unloading phases, as depicted in Figure 2(c),
316 where the compression force applied corresponds to the position of the helix at a given
317 depth. This loading/unloading is applied at five successive depths to simulate the installation
318 process. Only the structural elements of the screw anchors above this depth are activated,
319 which is similar to the press-replace method developed for displacement piles (Engin et al.
320 2015), where soil elements are progressively replaced by pile elements to simulate its
321 installation. The compressive stress bulb beneath a helix plate extended to approximately
322 $4D_h$ below it. Therefore, it was decided to apply a compression step every $1.5D_h$, to ensure
323 the soil would be relatively uniformly preloaded, while maintaining the complexity of the
324 mesh and computational time to a reasonable level. This distance is lower than the limit for
325 helix interaction in compression, equal to $2D_h$ (Al-Baghdadi 2018). A simulation based on 7
326 installation steps did not show any difference in the load-displacement relationship. The
327 crowd forces applied in these phases can be either predicted by the CPT method proposed in
328 (Davidson et al. 2018) or values from the installation rig.
329 ***Mesh influence***
330 Five different meshes with increasing number of elements were considered, to assess the
331 influence of the mesh size on the results of the stage 1 simulations. The overall number of
332 elements was set up by the user and the size of elements automatically adapted by the

333 software. The initial stiffness and hardening phases were very similar for the different
334 number of elements. Therefore, only the capacity at $0.1D_h$ and at peak were compared.
335 Results are reported in Table 5 and show that the peak capacity increases with the number
336 of elements and mesh refinement, although this increase is very small between meshes #4
337 and #5. The simulation related to the mesh 1 stopped converging before the end of the
338 simulation. The inspection of the shear strain field show that the shear band is narrower and
339 more marked as the mesh refinement increases, as would be expected. The overall
340 variability of the anchor capacity is limited, especially with respect to the variability that
341 could be expected for real case studies. The choice of a mesh was then based on the CPU
342 time required to obtain simulation results. The mesh #4 (3175 elements) was adopted as a
343 good balance between mesh refinement and calculation time.
344

345 ## VALIDATION AGAINST CENTRIFUGE TESTS

346 This section compares the numerical simulations with the centrifuge tests. The key variables
347 (stress and strain fields) are analysed to illustrate how the methodology was developed and
348 explain how it affects the final results.

349 ***Wished-in-place anchors (UWA)***

350 The enhancement of the capacity was validated first against wished-in-place tests of UWA.
351 The two-stage procedure was applied, but only the capacity was enhanced, as there was no
352 installation effect to take into consideration. The extent of the failure mechanism was
353 inspected in results from stage 1 and the softening zone was applied along the interface
354 elements in stage 2. In this case, this zone was around $2.5D_h$ in length. An example of the
355 load-displacement relationship is illustrated in Figure 3 and shows that the stiffness and
356 capacity are relatively consistent with the Stage 2 simulations, while Stage 1 overpredicts the

capacity. The peak capacity was identified for 5 different relative embedment ratios and compared in Figure 4 with centrifuge test reported by Hao et al. (2018). Results at shallow embedment ratios (≤ 9) are relatively consistent with the experimental results, particularly given the greater uncertainty in the selection of some specific soil parameters in these cases. The simulations at the largest relative embedment ratio overpredict the capacity, but a deep failure mechanism (e.g. Meyerhof and Adams (1968)) has clearly been reached in the centrifuge testing, which is out of scope of this study.

Anchors installed in-flight (UoD)

Figure 5 compares the measured prototype centrifuge uplift load with the total vertical reaction load at the top of the anchor shaft, F_y , obtained from the numerical simulations: purely wished-in-place (stage 1), enhanced capacity only (stage 2 – capacity) and full methodology (stage 2 – capacity/stiffness). All results are depicted as a function of the normalised vertical displacement u_y/D_h.

The initial stiffness of wished-in-place simulations (Stage 1) was relatively well captured by the different simulations although the different curves diverged rapidly (at approximately u_y/D_h =0.01) for the two single helix anchors embedded in very dense sand, as shown in Figure 5 (a, c). However, the maximum loads obtained numerically, corresponding to a fully formed failure mechanism, overpredicted the centrifuge test results in each case, from +25% (U1VD-A) to +43% (U1VD-B). They also overestimated the vertical displacement required to reach this maximum capacity, which was equal to 0.1Dh for the centrifuge tests and close to 0.25Dh for numerical simulations.

381 The enhanced capacity simulations (stage 2 – capacity), incorporating soil-soil interface
382 elements based on stage 1 results, show that the prediction of the uplift capacity was
383 considerably improved for single helix anchors (Figure 5 (a, c)), although the prediction for
384 the double helix case was strongly degraded (Figure 5 (d)). However, the initial stiffness was
385 underpredicted in very dense sand. Detailed discussion of the parameterisation of the soil-
386 soil interface elements resulting in the curves shown in Figure 3 is presented in the following
387 Discussion section.
388
389 Results of the simulations incorporating installation effects (stage 2 – capacity/stiffness)
390 were the most consistent with the centrifuge tests, as depicted in Figure 5. The load-
391 displacement relationship and initial stiffness were more consistent with the centrifuge tests
392 for both single helix anchors embedded in very dense sand compared to previous
393 predictions, as shown in Figure 5 (a, c). The initial stiffness was slightly overpredicted in the
394 medium dense case (Figure 5 (b)). The difference was more pronounced in the double helix
395 case (Figure 5 (d)) and the initial stiffness was almost identical for all three very dense
396 simulations.
397
398 The difference between all those simulations can be explained through the inspection of the
399 failure mechanism (capacity) and stress distribution (stiffness) around the anchor before and
400 at failure. This analysis is undertaken in the following. In addition, the procedure to inspect
401 Stage 1 results to derive Stage 2 simulations is detailed.
402

403 ## DISCUSSION

404 ### *Failure mechanisms*

405 Five distinct variables were considered to identify and interpret the uplift failure mechanism
406 for the wished-in-place (Stage 1) simulations. Two of these variables were cumulative over
407 the simulation, namely the vertical displacement u_y and shear strain γ_s, and were therefore
408 influenced by the complete deformation history of the screw anchor. The three other
409 variables were instantaneous for a given load step, namely the increments of vertical
410 displacement Δu_y and shear strain $\Delta\gamma_s$, and the current plastic points (PP, i.e. integration
411 point reaching the plastic yield surface). These variables have been used previously to
412 interpret the failure mechanism of plate anchors embedded in sand (Cerfontaine et al. 2019)
413 and are depicted in Figure 6 for the single deep helix anchor embedded in very dense sand
414 (U1VD-B) as an example. The results show the progressive formation of the failure
415 mechanism, which had not been constrained by soil-soil interface elements at this stage.
416
417 Figure 6(a) describes the state of the soil after applying the (maximum, last recorded) crowd
418 force at the end of installation and unloading to zero compression. It indicates that shear
419 bands pointing towards the developed during the first phase were reactivated (in the
420 opposite direction) during uplift. After 0.1-0.2D_h imposed uplift displacement, the failure
421 mechanism was not fully formed as shown in Figure 6(b and c). Several shear bands seemed
422 to initiate from the helix edge at different orientations. The failure mechanism observed in
423 this study was fully formed after a displacement equal to 0.3D_h and corresponded to a
424 shallow wedge of soil (i.e. shallow failure mechanism).
425
426 The conical shape of this shallow failure mechanism is consistent with previous experimental
427 studies undertaken for buried anchors (e.g. Ilamparuthi and Muthukrishnaiah 1999; Liu *et al.*
428 2012) where image analysis of the failure mechanism through a Perspex face was

429 undertaken and analytical approaches (e.g. Das and Shukla 2013). However, the exact
430 inclination of this conical mechanism previously reported varied from study-to-study, as
431 described in Cerfontaine et al. (2019) for plate anchors. For the screw anchors considered
432 here, the failure mechanism diverged slightly from a straight line and its orientation was
433 close to the assumed mechanism from Giampa *et al*. (2017), i.e. inclined at the dilatancy
434 angle (ψ'_{pk} =17° for the very dense sand, indicated by a dashed line in Figure 6) to the vertical
435 direction. This inclination appears consistent with previous theoretical analyses for shallow
436 anchors (Vermeer and Sutjiadi 1985) and experimental evidence for uplifting pipelines
437 (White et al. 2008). Similar conclusions were drawn from interpretation of the medium-
438 dense sand results (not shown). It is noted though that these additional studies do not
439 include installation effects, but still provide some insights into potential failure mechanisms
440 that may be expected in uplift. It is also noted that specific effects of soil density changes
441 due to installation and their subsequent potential effects on the nature of the failure
442 mechanism may not be fully captured in these studies.
443 The failure mechanism of multi-helix anchors depends on the inter-helix spacing. If two
444 adjacent helices of identical diameter are sufficiently close, a cylindrical failure surface,
445 whose diameter is equal to the helix diameter, is assumed to form between them in tension
446 or compression (Tsuha et al. 2007; 2012; Knappett et al. 2014; Al-Baghdadi et al. 2017a). At
447 greater spacing, the helices may act independently. The evolution of the failure mechanism
448 is depicted in Figure 7 at different time steps for the double helix case (U2VD). The failure
449 mechanism occurred for a lower imposed vertical displacement ($0.1D_h$) than the single helix
450 case. It consisted of an inter-helix failure plane and a shallow wedge mechanism, which was
451 oriented along the proposed failure mechanism of Giampa et al. (2017). Figure 7(b-c) show
452 that there was a competition between several shear bands during the uplift of the screw

453 anchor. Additional shear bands were initiated at the edge of the bottom helix or at a position
454 in between the two helices, but they did not reach the surface. In summary, it is clear that
455 for a multi-helix anchor, the embedment depth of the upper helix plate appears to control
456 the apparent wedge-shaped uplift mechanism observed in this study and that at lower
457 displacements there is fluctuation between a cylindrical mechanism and wedging emanating
458 from the lower helix.
459
460 The inspection of results presented in Figure 6 and Figure 7 was used to define the soil-soil
461 interface geometry of stage 2 (enhanced capacity). This allowed the modelling of a greater
462 slip deformation at failure without excessive mesh distortion and to allow strain-dependent
463 softening (at failure) to be incorporated. For single helix anchors, the soil-soil interface
464 elements were inclined at the dilatancy angle to the vertical direction as per (Giampa et al.
465 2017) (shallow wedge). For the double helix case, the interface was set-up similarly from the
466 upper helix, while a cylindrical failure mechanism (vertical interface elements) was enforced
467 between the lower and upper helices.
468
469 Figure 6 shows that large shear strain developed along the failure mechanism in stage 1. It
470 was greater than 30% close to the anchor edge and decreased up to a normalised distance
471 along the failure mechanism ξ/D_h of approximately 2. The distribution then decreased almost
472 linearly up to the surface. Results of experimental triaxial tests (Robinson 2016) as well as
473 direct shear tests reported by Al-Defae et al. (2013) suggest that HST95 sand appears to
474 soften at shear strains greater than 2-3% for medium-dense to dense sand. A larger shear
475 strain is necessary (>10%) before reaching the critical state, depending on the soil density
476 and confinement. Consequently, soil-soil interface properties in the zone closest to the

anchor, namely the softening zone, considered that critical state strength was mobilised within the interface after peak. The length of this softened zone was based on the analysis of shear strain contour results from the stage 1 analysis (rather than by back-fitting empirically to match the centrifuge measured capacity). This was approximately $2D_h$ for screw anchors in very dense sand and $2.5D_h$ in medium dense sand. Beyond this zone, the interface properties were identical to the virgin soil properties. It is verified that the pre-definition of a failure-mechanism does not create a new global failure pattern. This is shown in Figure 8 for the single helix case (U1VD-B), where the plastic points, shear strain and vertical displacement all described a wedge failure mechanism whose shape is identical to the pre-defined one.

Stress distribution along the failure mechanism

Most analytical approaches to screw anchor design consider that failure in uplift occurs between rigid soil blocks and assumes a normal shear stress distribution, based on peak friction angle, increasing linearly with depth (Ghaly et al. 1991b; Giampa et al. 2017). However, the soil is far from rigid and significant vertical displacement was required to fully mobilise the failure mechanism, as shown in Figure 5. Subsequently, the load applied by the helix on the soil generated vertical strain. Lateral strain was constrained by the surrounding soil, increasing the lateral stress distribution, as shown numerically by Cerfontaine et al. (2019) for plate anchors or experimentally for screw piles in a pressure chamber (Nagata and Hirata 2005; Nagai et al. 2018). The stress distributions around the anchor and along the slip surface were then modified, such that the normal and shear stresses at failure were increased. Figure 9 (a and b) show the normal and shear stress distributions along the slip surface (inclined at $\theta = 17°$ to the vertical) for the single helix anchor in very dense sand

(U1VD-B) for the wished-in-place (Stage 1) simulation. The results are plotted as a function of the normalised distance ξ/D_h from the edge of the helix, in the direction of the slip surface. The results are normalised with respect to the maximum normal and shear stresses assumed in the approach proposed by (Giampa et al. 2018b) since their failure mechanism is identical to the one observed in this study, where:

$$\tau_{G,max} = \tan\phi'_{pk}\,\sigma'_{N,G,max} = \tan\phi'_{pk}\cos\left(\phi'_{pk} - \psi'_{pk}\right)\gamma' H \quad (0)$$

From in Figure 9 (a and b) the maximum values measured were several times those assumed in the (Giampa et al. 2018b) approach (which assumes a rigid block of soil), even after small vertical displacements.

The stress distribution along the interface is compared for both stages 1 and 2 in Figure 10. Results show that both normal and shear stress distributions are modified (reduced in magnitude) in the softening zone. However, the decrease is more significant for the shear stresses as they are both (i) proportional to the reduced normal effective stresses and (ii) the friction angle is reduced to critical state. Finally, both stress distributions are significantly different from the linear distribution assumed by Giampa et al. (2017, 2018b) (even if the uplift capacity is well approximated) or any other analytical methods. This indicates that the FE method may be preferable to analytical methods, even if only capacity is of interest.

Depth and density effect

523 Additional simulations for relative embedment ranging between $1 \leq H/D_h \leq 8$ for relative
524 densities between 57-84% were conducted to increase the generality of previous
525 observations. Cross-sections along failure planes inclined at the dilatancy angle to the
526 vertical (dilatancy angle is a function of relative density) at each embedment ratio are
527 compared in Figure 11 for D_r = 84% (as an example). Figure 11(a-b) show that the maximum
528 normal and shear stress at failure increase with depth, which is consistent with observations
529 made by Cerfontaine et al. (2019) for plate anchors.
530
531 The length of the shear band where high shear strain occurs was assessed through a
532 systematic analysis of the shear strain output (cross-sectional strain contour plot such as
533 Figure 6) at failure. A threshold of shear strain above which strain-softening was expected to
534 develop was established, equal to 10% for all simulations and corresponding to the shear
535 strain required to reach the critical state at these densities. The equivalent length of the
536 assumed failure mechanism along which softening occurred is shown in Figure 12. This figure
537 shows that the length of the softening zone was almost equal to zero at H/D_h=1 and
538 increased linearly up to a certain depth (H/D_h = 3 and 4 for very dense and medium dense
539 sand respectively). Above these normalised depths, the softening zone length appeared to
540 be constant, although some scatter was observed.
541
542 The procedure (addition of soil-soil interface elements) was applied to a single helix screw
543 anchor embedded in both sand densities for a varying embedment ratio. The length of the
544 softening zone was based on results presented in Figure 12. Results in Figure 13 show that
545 the stage 2 simulations generate a significant decrease in bearing capacity. A comparison
546 with the uplift capacity obtained through the approach of Giampa *et al*. (2017) shows that it

547 is consistent with the numerical results, even at larger relative embedment ratios, for a D_r =
548 84%, although it should be noted that the postulated stress distribution in that method is
549 different.
550
551 ***Installation effect***
552 The installation procedure mainly affected the stiffness for single plate screw anchors, rather
553 than the capacity, as shown in Figure 5 by comparing the two stage 2 FE curves. In addition,
554 Table 6 shows that the magnitude of the compression load has a limited impact on the
555 ultimate uplift capacity for the single helix screw anchor. An increase or decrease of the
556 crowd force by 50% over the whole installation process, generates only a variation of 7% in
557 the uplift capacity. However, the stiffness is affected by this crowd force magnitude. This can
558 be mechanically explained through the analysis of the unloading/reloading Young modulus
559 E_{UR} and the average stress fields induced around the anchor just before uplifting which are
560 shown in Figure 14.
561
562 The large compression (crowd) force applied during installation had several consequences.
563 Firstly, the soil was sheared over a zone of soil that was several helix diameters in size. As
564 the soil was strained, its secant stiffness decreased (beyond the range of small-strain
565 stiffness). After the soil was loaded in compression up to a deviatoric stress q_{comp} (as shown
566 in Figure 15(a)), the yield surface hardened, and its unloading stiffness was based on the E_{UR}
567 modulus. Consequently, the reloading of the soil during the uplift phase will follow the same
568 path up to q_{comp} and will be much stiffer than a stress-strain path starting at the origin of the
569 axes.
570

571 Secondly, the stress field around the anchor was modified by the compressive crowd load, as
572 can be observed in Figure 14(c, d). Consequently, the strength and stiffness increased, as
573 they were a function of the average stress, as illustrated in Figure 11(b) and in the following
574 evolution of the unloading/reloading modulus E_{ur} definition

$$E_{ur}\left(p'\right)=E_{ur}^{ref}\left(\frac{p'}{p'_{ref}}\right)^{m} \quad (0)$$

575 where E_{ur}^{ref} is the reference modulus for $p'_{ref}=100\,kPa$, *p'* is the average stress and *m* is a
576 material parameter. The consequence of these combined effects is a very complex pattern of
577 operative stiffness all around the anchor prior to uplift, as depicted in Figure 14(a, b).
578 However, it is clear that the stiffness above the anchor, in a zone delimited by the expected
579 failure mechanism (dashed line), was larger if the entire installation process was accounted
580 for (stage 2), rather than only the last recorded compression load (stage 1).
581
582 It should be noted that the installation simulation did not modify the shape of the failure
583 mechanism. Additional uplift simulations were run, incorporating the installation simulation,
584 but with no pre-defined mechanism. The observed failure mechanism was identical to that
585 from the stage 1 simulation.
586
587 ***Cylindrical failure mechanism***
588 Schiavon (2016) and Perez et al. (2018) recently investigated the disturbance effect around
589 screw anchors in centrifuge tests. The authors carried out micro-tomographic analyses of the
590 sand around the screw anchor and identified that the vertical soil column above the helix
591 was highly disturbed (lower density). They concluded that the failure mechanism should be a
592 vertical cylindrical failure whose section is identical to the area of the helix. This result is

consistent with experiments undertaken in calibration chambers (Nagata and Hirata 2005; Nagai et al. 2018), which exhibit a cylindrical failure mechanism, although the pressurised calibration chamber process impedes the development of any shallow failure mechanism. To replicate this mechanism, Perez et al. (2018) introduced two cylindrical zones of soil in their finite element simulations, whose properties where back-calculated to reproduce the centrifuge tests. The friction angles leading to the best fit of the experimental results were close to the critical state friction angle.

The cylindrical failure mechanism hypothesis has been tested in the following with or without an installation process. Three scenarios incorporating a pre-defined cylindrical failure mechanism, were compared with reference simulations for the U1VD-A case in Figure 16. The first simulation included a cylindrical failure mechanism using a reduced friction angle ($\phi_r = 40°$), lying between the undisturbed peak and the critical state friction angle. Results show that the load-displacement relationship was similar to the stage 1 simulation where there is no pre-defined failure mechanism at all. This was corroborated by the inspection of the failure mechanism (shear strain), which showed a conical pattern as before. Two other simulations adopted the same cylindrical failure mechanism as per micro-tomographic observations of Schiavon (2016) but used the critical state friction angle along the cylindrical failure mechanism, which would be consistent with a highly disturbed zone of soil. In this case, modelling the crowd-force installation effects, i.e. combining density and stress installation disturbance, makes a significant difference to the capacity obtained (Figure 16, with installation, 1MN, without, 5MN), but the maximum capacity is still lower than both the reference simulation and the centrifuge results.

In summary, the centrifuge results obtained at the University of Dundee and presented in (Davidson et al. 2019) are better approximated by a conical shallow failure mechanism while

617 a cylindrical failure mechanism gives a better approximation of the results for the numerical
618 simulations of Pérez et al. (2018). These two possibilities are not necessarily mutually
619 exclusive. Large geometries representative of the offshore requirements were used in this
620 study while Pérez et al. (2018) presented results for typical onshore piles, which are much
621 smaller. This difference in scale and in geometry (D_h/D_c ratio, tip shape) can lead to different
622 stress distribution or disturbance around the anchor and generate different failure
623 mechanism. In any case, the principal benefit of the new two-stage approach over that
624 proposed by Perez et al. (2018) is that there is no need to assume a priori empirically-
625 derived strength reduction factors as the final simulation is informed by directly measured
626 soil parameters, the results of the stage 1 WIP simulation and an explicit (though
627 approximate) simulation of the installation process. Further research is necessary to improve
628 the methodology proposed here, for instance by incorporating density variations resulting
629 from the installation process, i.e. the shaft and helix penetration.
630
631 ***Application in engineering design***
632 The two-stage simulation process presented herein can in principle be applied to any soil
633 profile and can provide the full load-displacement curve, allowing both uplift capacity and
634 stiffness at working load to be assessed. The process can be summarised by the following
635 steps:
636
637 1. Determine the crowd force required to install the screw anchor as a function of
638 depth, using a methodology previously developed (Davidson et al. 2018);
639 2. Conduct an uplift simulation (stage 1) of the screw anchor in the 'wished-in-place'
640 configuration;

3. Assess the shear band pattern from stage 1 output and the distance over which softening should take place based on the induced shear stresses, with respect to laboratory test results for the soil in question (e.g. direct shear test);
4. Modify the stage 1 model (from (2)) to include a multi-step press-replace procedure (informed by predicted crowd forces from (1)) followed by the addition of soil-soil interfaces with appropriate softening behaviour at the location of the shear bands (from (3)) to the final (installed) anchor configuration;
5. Run the stage 2 model to determine the anchor performance (load-displacement relationship).

It should be noted that this procedure has only been validated here for large dimension screw anchors (representative of offshore applications) embedded in uniform deposits of sand at a relatively shallow depth ($H/D_h \leq 8$). In such deposits, as a first approximation, the process might be shortened by defining directly the failure mechanism as a shallow wedge whose inclination to the vertical is equal to the dilatancy angle and defining the reduced strength distance for the soil-soil interface based on Figure 15. This would have the effect of removing stage 1. If the uplift capacity only is required (e.g. in initial Front-End Engineering Design), the step preloading phase might also be neglected as a first approximation for single helix anchors.

CONCLUSION

In this paper, a numerical methodology, based on the Finite Element (FE) method, has been derived to enable predictions of the entire load-displacement relationship (including the stiffness at working load and uplift capacity) of screw anchors embedded in sand. It meets a

need to provide improved prediction of uplift capacity (which is significantly overestimated using existing analytical methods) identified from the literature, which is required for anchor sizing, and additionally provides information on (non-linear) anchor axial stiffness which controls the global rotational deformation of a jacket structure or tension-leg platforms. This methodology is applicable in principle to any screw anchor geometry and ground conditions and can be fully parametrised based on basic soil element testing and in-situ (CPT) tests in sands. Installation-induced initial conditions within the soil can be approximated using predicted crowd forces, based either on CPT data using a previously developed prediction method, or from crowd force measurements taken from the installation records in the field.

The predictions of screw anchor tensile uplift performance were consistent with centrifuge test results, with or without installation effects, that were previously published in the literature. The FE analyses revealed that, as a significant vertical displacement is required to fully form the failure mechanism, high induced shear strain along a part of the failure mechanism close to the helix is such that critical state should be reached. The numerical results also showed that the compression (crowd) load applied during the screw anchor installation phase modifies the stress field around the anchor, which in turn affects the anchor uplift stiffness.

The methodology developed in this paper, enables the prediction of uplift capacity (ultimate limit state) and stiffness (serviceability limit state), accounting for installation effects in an approximate way without empirical modifications to soil properties, and so can be used to assess screw anchor performance using commercially available FE software. This approach could lead to cost reduction, more reliable and efficient screw anchor design, enabling the

689 generalisation of this anchorage solution for applications in offshore geotechnical
690 engineering.
691

692 ## ACKNOWLEDGEMENTS

693 This project has received funding from the European Union's Horizon 2020 research and
694 innovation programme under the Marie Skłodowska-Curie grant agreement No 753156. The
695 authors would like to acknowledge the support of the Engineering and Physical Science
696 Research Council (EPSRC) (Grant no. EP/N006054/1: Supergen Wind Hub Grand Challenges
697 Project: Screw piles for wind energy foundations). The 5th author would like to acknowledge
698 the financial support of the Iraqi Ministry of higher Education of Scientific Research
699 (MOHESR). Elements of this work were undertaken using facilities developed as part of the
700 ERDF-funded Scottish Marine & Renewables Test Centre (SMART) at the University of
701 Dundee.
702
703

704 ## SYMBOLS

A	Helix area (including core area)
d_{50}	Is the size of particles such that 50% of the particles are smaller than this size.
D_c	Core diameter
D_h	Helix diameter
D_r	Relative density
E_{ur}, E_{ur}^{ref}	Unloading/reloading Young modulus and reference Young modulus respectively
FE	Finite element
F_y	Vertical load applied at the top of the screw anchor (positive in tension)
H	Helix embedment depth
I_R	Relative dilatancy index, (Bolton 1986)
m	Material parameter of the HSsmall model
MD	Medium-dense sand (D_r =57%, UoD test)
N_γ	Non-dimensional uplift bearing factor
p'	Average stress
p'_{ref}	Reference pressure for the determination of stress dependent stiffness in the HSsmall model

u_y	Vertical displacement measured at the top of the screw anchor
VD	Very-dense sand (D_r = 84%, UoD test)
γ'	Buoyant unit weight
γ_s	Shear strain
$\gamma_{s,th}$	Threshold of shear strain at which critical state is supposed to be reached
$\Delta\gamma_s$	Increment of shear strain over a time step
Δu_y	Increment of vertical displacement of a time step
θ	Inclination to the vertical direction of the theoretical straight failure plane emanating from the anchor edge
ξ	Normalised distance from the edge of the anchor along the direction of the theoretical straight failure plane
σ'_h	Horizontal effective stress within the soil
σ'_N	Normal effective stress along any cross-section within the soil
$\sigma'_{N,G}$	Normal effective stress along the theoretical failure plane according to (Giampa et al. 2017)
τ	Shear stress along any cross-section within the soil
τ_G	Shear stress along the theoretical failure plane according to (Giampa et al. 2017)
τ_{rel}	Mobilised shear stress, ratio of the current to maximum shear stress
ϕ'_{cv}	Critical state friction angle
ϕ'_{pk}	Peak friction angle
ϕ'_r	Residual friction angle
ψ'_{pk}	Peak dilation angle

REFERENCES

Achmus, M., Kuo, Y.-S.S., and Abdel-Rahman, K. 2009. Behavior of monopile foundations under cyclic lateral load. Computers and Geotechnics, **36**(5): 725–735. doi:10.1016/j.compgeo.2008.12.003.

Al-Baghdadi, T. 2018. Screw piles as offshore foundations : Numerical and physical modelling. PhD Thesis, University of Dundee, UK.

Al-Baghdadi, T.A., Brown, M.J., Knappett, J.A., and Al-Defae, A.H. 2017a. Geotechnical engineering effects of vertical loading on lateral screw pile performance. Proceedings of the Institution of Civil Engineers: Geotechnical Engineering, **170**(3): 259–272. doi:10.1680/jgeen.16.00114.

Al-Baghdadi, T.A., Davidson, C., Brown, M.J., Knappett, J.A., Brennan, A., Augarde, C., Coombs, W., and Wang, L. 2017b. CPT based design procedure for installation torque prediction for screw piles installed in sand. 8th International Conference on Offshore Site Investigation & Geotechnics, (1): 346–353. Society for Underwater Technology, London, UK.

Al-Defae, A.H.H., Caucis, K., and Knappett, J.A.A. 2013. Aftershocks and the whole-life seismic performance of granular slopes. Géotechnique, **63**(14): 1230–1244. Thomas Telford Ltd.

doi:10.1680/geot.12.P.149.

Anastasopoulos, I., Gazetas, G., Asce, M., Bransby, M.F., Davies, M.C.R., and Nahas, a El. 2007. Fault Rupture Propagation through Sand : Finite-Element. Journal of Geotechnical and Geoenvironmental Engineering, **133**(August): 943–958. doi:10.1061/(ASCE)1090-0241(2007)133:8(943).

Bachynski, E.E., and Moan, T. 2014. Ringing loads on tension leg platform wind turbines. Ocean Engineering, **84**: 237–248. Elsevier. doi:10.1016/j.oceaneng.2014.04.007.

Bailey, H., Senior, B., Simmons, D., Rusin, J., Picken, G., and Thompson, P.M. 2010. Assessing underwater noise levels during pile-driving at an offshore windfarm and its potential effects on marine mammals. Marine Pollution Bulletin, **60**(6): 888–897. doi:10.1016/j.marpolbul.2010.01.003.

Bolton, M.D. 1986. The strength and dilatancy of sands. Géotechnique, **36**(I): 65–78.

Byrne, B.W., and Houlsby, G.T. 2015. Helical piles: an innovative foundation design option for offshore wind turbines. Philosophical Transactions of the Royal Society A: Mathematical, Physical & Engineering Sciences, **373**(February): 1–11. doi:10.1098/rsta.2014.0081.

Cerfontaine, B., Knappett, J.A., Brown, M.J., and Bradshaw, A.S. 2019. Effect of soil deformability on the failure mechanism of shallow plate or screw anchors in sand. Computers and Geotechnics, **109**(May): 34–45. doi:https://doi.org/10.1016/j.compgeo.2019.01.007.

Das, B.M., and Shukla, S.K. 2013. Earth anchors. J. Ross, Plantation, Florida.

Davidson, C., Al-Baghdadi, T., Brown, M., Brennan, A., Knappett, J., Augarde, C., W., C., Wang, L., Richards, D., Blake, A., and Ball, J. 2018. A modified CPT based installation torque prediction for large screw piles in sand. *In* Cone Penetration Testing. *Edited by* M. Hicks, F. Pisanò, and J. Peuchen. Delft, The Netherlands.

Davidson, C., Brown, M.J., Brennan, A.J., Knappett, J.A., Cerfontaine, B., and Sharif, Y.U. 2019. Physical modelling of screw piles for offshore wind energy. *In* First International Symposium on Screw Piles for Energy Applications. *Edited by* C. Davidson, M.J. Brown, J.A. Knappett, A.J. Brennan, C. Augarde, W. Coombs, L. Wang, D. Richards, D.J. White, and A. Blake. University of Dundee, Dundee, UK.

Davidson, C., Brown, M.J., Cerfontaine, B., Al-Baghdadi, T., Knappett, J., Brennan, A., Augarde, C., Coombs, W., Wang, L., Blake, A., Richards, D., and Ball, J. 2020. Physical modelling to demonstrate the feasibility of screw piles for offshore jacket supported wind energy structures.

(submitted for consideration in) Géotechnique,.

Desrues, J., and Viggiani, G. 2004. Strain localization in sand: an overview of the experimental results obtained in Grenoble using stereophotogrammetry. International Journal for Numerical and Analytical Methods in Geomechanics, **28**(4): 279–321. doi:10.1002/nag.338.

Dickin, E.A. 1988. Uplift behaviour of horizontal anchor plates in sand. Journal of Geotechnical and Geoenvironmental Engineering, **114**(11): 1300–1317.

Engin, H.K., Brinkgreve, R.B.J., and van Tol, A.F. 2015. Simplified numerical modelling of pile penetration - the press-replace technique. International Journal for Numerical and Analytical Methods in Geomechanics, **39**(March): 1713–1734. doi:10.1002/nag.2736.

Garnier, J., Gaudin, C., Springman, S.M., Culligan, P.J., Goodings, D., Konig, D., Kutter, B., Phillips, R., Randolph, M.F., Thorel, A., Garnier, J., Gaudin, C., Springman, S.M., Culligan, P.J., Goodings, D., Konig, D., Kutter, B., Phillips, R., Randolph, M.F., and Thorel, L. 2007. Catalogue of scaling laws and similitude questions in geotechnical centrifuge modelling. International Journal of Physical Modelling in Geotechnics, **7**(3): 01–23. doi:10.1680/ijpmg.2007.070301.

Gavin, K., Doherty, P., and Tolooiyan, A. 2014. Field investigation of the axial resistance of helical piles in dense sand. Canadian Geotechnical Journal, **51**(11): 1343–1354. doi:10.1139/cgj-2012-0463.

Ghaly, A., Hanna, A., and Hanna, M. 1991. Uplift behaviour of screw anchor in sand, I dry sand. Journal of Geotechnical Engineering, **117**(5): 773–793.

Giampa, J., Bradshaw, A., and Schneider, J. 2017. Influence of Dilation Angle on Drained Shallow Circular Anchor Uplift Capacity. International Journal of Geomechanics, **17**(2): 4016056. doi:10.1061/(ASCE)GM.1943-5622.0000725.

Giampa, J.R., Bradshaw, A., Gerkus, H., Gilbert, R.B., Gavin, K.G., and Sivakumar, V. 2018a. The effect of shape on the pullout capacity of shallow plate anchors in sand. Géotechnique,.

Giampa, J.R., Bradshaw, A.S., and Schneider, J.A. 2018b. Erratum for “Influence of Dilation Angle on Drained Shallow Circular Anchor Uplift Capacity” by Joseph R. Giampa, Aaron S. Bradshaw, and James A. Schneider. International Journal of Geomechanics, **18**(11): 08218002. doi:10.1061/(asce)gm.1943-5622.0001329.

Gudehus, G., and Nübel, K. 2004. Evolution of shear bands in sand. Géotechnique, **54**(3): 187–201. doi:10.1680/geot.54.3.187.36346.

Hao, D., Wang, D., O'Loughlin, C.D., Gaudin, C., O'Loughlin, C.D.C.D., and Gaudin, C. 2018. Tensile monotonic capacity of helical anchors in sand: interaction between helices. Canadian Geotechnical Journal (in press),. doi:10.1139/cgj-2018-0202.

Houlsby, G.T. 2016. Interactions in offshore foundation design. Géotechnique, **66**(10): 791–825. doi:10.1680/jgeot.15.RL.001.

Ilamparuthi, K., Dickin, E.A., and Muthukrisnaiah, K. 2002. Experimental investigation of the uplift behaviour of circular plate anchors embedded in sand. Canadian Geotechnical Journal, **39**: 648–664. doi:10.1139/t02-005.

Ilamparuthi, K., and Muthukrishnaiah, K. 1999. Anchors in sand bed: Delineation of rupture surface. Ocean Engineering, **26**(12): 1249–1273. doi:10.1016/S0029-8018(98)00034-1.

Jaky, J. 1944. The coefficient of earth pressure at rest. Journal of the Society of Hungarian Architects and Engineers, **78**(5): 355–358.

Klinkvort, R.F., Hededal, O., and Springman, S.M. 2013. Scaling issues in centrifuge modelling of monopiles. International Journal of Physical Modelling in Geotechnics, **13**(2): 38–49. doi:http://dx.doi.org/10.1680/ijpmg.12.00010.

Knappett, J.A., Brown, M.J., Brennan, A.J., and Hamilton, L. 2014. Optimising the compressive behaviour of screw piles in sand for marine renewable energy applications. *In* International Conference on Piling and Deep foundations. Stockholm, Sweden.

Knappett, J.A., Caucis, K., Brown, M.J., Jeffrey, J.R., and Ball, J.D. 2016. CHD pile performance: part II – numerical modelling. Proceedings of the Institution of Civil Engineers - Geotechnical Engineering, **169**(5): 436–454. doi:10.1680/jgeen.15.00132.

Lauder, K.D., Brown, M.J., Bransby, M.F., and Boyes, S. 2013. The influence of incorporating a forecutter on the performance of offshore pipeline ploughs. Applied Ocean Research, **39**: 121–130. Elsevier Ltd. doi:10.1016/j.apor.2012.11.001.

Lauder, K.D., Brown, M.J., Bransby, M.F., and Gooding, S. 2012. Variation of tow force with velocity during offshore ploughing in granular materials. Canadian Geotechnical Journal, **49**(11): 1244–1255. doi:10.1139/t2012-086.

Li, Z., Haigh, S.K., and Bolton, M.D. 2010. Centrifuge modelling of mono-pile under cyclic lateral loads. Proceedings of the 7th International Conference on Physical Modelling in Geotechnics, **2**: 965–970. doi:10.1680/ijpmg.2010.10.2.47.

812 Liu, J.Y., Liu, M.L., and Zhu, Z.D. 2012. Sand Deformation around an Uplift Plate Anchor. Journal of
813 Geotechnical and Geoenvironmental Engineering, **138**(6): 728–737. doi:Doi
814 10.1061/(Asce)Gt.1943-5606.0000633.

815 Livneh, B., and El Naggar, M.H. 2008. Axial testing and numerical modeling of square shaft helical
816 piles under compressive and tensile loading. Canadian Geotechnical Journal, **45**: 1142–1155.
817 doi:10.1139/T08-044.

818 Meyerhof, G.G., and Adams, J.I. 1968. The ultimate uplift capacity of foundations. Canadian
819 Geotechnical Journal, **5**(4): 225–244.

820 Mitsch, M.P., and Clemence, S.. 1985. The uplift capacity of helix anchors in sand. *In* Uplift behavior
821 of anchor foundations in soil. Proceedings of the ASCE. New-York, USA. pp. 26–47.

822 Mosquera, Z.S.Z., Tsuha, H.C., Schiavon, J.A., and Thorel, L. 2015. Discussion of Field investigation of
823 the axial resistance of helical piles in dense sand. Canadian Geotechnical Journal, **52**(11): 1190–
824 1194. doi:10.1139/cgj-2012-0463.

825 Nagai, H., Tsuchiya, T., and Shimada, M. 2018. Influence of installation method on performance of
826 screwed pile and evaluation of pulling resistance. Soils and Foundations, **58**(2): 355–369.
827 Elsevier B.V. doi:10.1016/j.sandf.2018.02.006.

828 Nagata, M., and Hirata, H. 2005. Study on Uplift Resistance of Screwed Steel Pile. (92): 73–78.

829 Newgard, J.T., Schneider, J. a., and Thompson, D.J. 2015. Cyclic response of shallow helical anchors in
830 a medium dense sand. *In* Frontiers in Offshore Geotechnics III. Taylor & Francis Group, London,
831 Oslo, Norway. pp. 913–918.

832 Papadopoulou, K., Saroglou, H., and Papadopoulos, V. 2014. Finite Element Analyses and
833 Experimental Investigation of Helical Micropiles. Geotechnical and Geological Engineering,
834 **32**(4): 949–963. doi:10.1007/s10706-014-9771-6.

835 Pérez, Z.A., Schiavon, J.A., Tsuha, C.H.C., Dias, D., and Thorel, L. 2018. Numerical and experimental
836 study on the influence of installation effects on the behaviour of helical anchors in very dense
837 sand. Canadian Geotechnical Journal, **55**(8): 1067–1080. doi:10.1139/cgj-2017-0137.

838 Perko, H.A. 2000. Energy method for predicting installation torque of helical foundations and
839 anchors. ASCE Geotechnical Special Publication,: 1–11. doi:10.1061/40511(288)24.

840 Perko, H.A. 2009. Helical Piles: A Practical Guide to Design and Installation. *In* 1st Edit. John Wiley &
841 Sons.

PLAXIS. 2017a. PLAXIS 2D Reference Manual. Delft, The Netherlands.

PLAXIS. 2017b. PLAXIS Material Models Manual. Delft, The Netherlands.

Robinson, S. 2016. Internal report for project Seabed Ploughing : Modelling for Infrastructure EP/M000362/1. Dundee, UK.

Schanz, T. 1998. Zur Modellierung des Mechanischen verhaltens von Reibungsmaterialen. Universität Stuttgart, Germany.

Schanz, T., Vermeer, A., and Bonnier, P. 1999a. The hardening soil model: formulation and verification. *In* Beyond 2000 Comput. Geotech. 10 years PLAXIS. Amsterdam, The Netherlands. pp. 281–296.

Schanz, T., Vermeer, A., and Bonnier, P. 1999b. The hardening soil model: formulation and verification. Beyond 2000 Comput. Geotech. 10 years PLAXIS Int. Proc. Int. Symp. beyond 2000 Comput. Geotech. Amsterdam Netherlands 1820 March 1999,: 281.

Schanz, T., and Vermeer, P.A. 1996. Angles of friction and dilatancy of sand. Géotechnique, **46**(1): 145–151.

Schiavon, J.A. 2016. Comportamento de ancoragens helicoidais submetidas a carregamentos cíclicos. PhD Thesis. University of São Paulo, Brazil.

Sharif, Y.U., Brown, M.J., Ciantia, M.O., Knappett, J.A., Davidson, C., Cerfontaine, B., and Robinson, S. 2019. Numerically modelling the installation and loading of screw piles using DEM. *In* Proceedings of the International Symposium on Screw Piles for Energy Applications. Dundee, UK.

Sutherland, H.B. 1965. Model Studies for Shaft Raising through Cohesionless Soils. *In* Proceedings of the 6th International Conference on Soil Mechanics and Foundation Engineering, Montréal. Montreal, Canada. pp. 410–413.

Tappenden, K.M. 2007. Predicting the axial capacity of screw piles installed in Canadian soils. Msc Thesis, University of Alberta.

Tsuha, C.H.C., Aoki, N., Rault, G., Thorel, L., and Garnier, J. 2007. Physical modelling of helical pile anchors. International Journal of Physical Modelling in Geotechnics, **494**(4): 1–12.

Tsuha, C.H.C., Aoki, N., Rault, G., Thorel, L., and Garnier, J. 2012. Evaluation of the efficiencies of helical anchor plates in sand by centrifuge model tests. Canadian Geotechnical Journal, **49**(9): 1102–1114. doi:Doi 10.1139/T2012-064.

Tucker, K.. 1987. Uplift capacity of drilled shafts and driven piles in granular materials. *In* Foundations for transmission line towers. pp. 142–159.

Vermeer, P.A., and Sutjiadi, W. 1985. The uplift resistance of shallow embedded anchors. *In* Proc., of 11th Int. Conf. of Soil Mechanics and Foundation Engineering. Balkema, Rotterdam, The Netherlands, San Francisco, USA. pp. 1635–1638.

Wang, L., Coombs, W.M., Augarde, C.E., Brown, M., Knappett, J., Brennan, A., Richards, D., and Blake, A. 2017. Modelling Screwpile Installation Using the MPM. Procedia Engineering, **175**: 124–132. Elsevier B.V. doi:10.1016/j.proeng.2017.01.040.

White, D.J., Cheuk, C.Y., and Bolton, M.D. 2008. The uplift resistance of pipes and plate anchors buried in sand. Géotechnique, **58**(10): 771–779. doi:10.1680/geot.2008.3692.

Zienkiewicz, O.C., and Taylor, R.L. 2000. The finite element method (vol. 2): Solid mechanics. *In* Vasa, Fifth Edit. Butterworth-Heineman, Oxford, UK.

FIGURE CAPTION LIST

Figure 1 Comparison of centrifuge tests with respect to relatively large scale 1g, centrifuge and field experimental results, for plate anchors (wished in place, open markers) and screw anchors (installation effect, closed markers). Centrifuge and field tests are underlined by solid and dashed lines respectively. Single and double refer to the number of helices. The Giampa et al. (2017) criterion is calculated for very dense (VD) and medium-dense (MD) soil properties.

Figure 2 Schematic description of the multi-stage methodology

Figure 3 Comparison of the load-displacement relationship for the wished in place centrifuge tests (H/D_h = 6) in dense sand from (Hao et al. 2018) and numerical simulations (Stage 1 & Stage 2 – capacity)

Figure 4 Comparison of wished in place centrifuge tests in dense sand from (Hao et al. 2018) and numerical simulations (Stage 2 – capacity). The two sets of parameters used to calculate the analytical criterion of Giampa et al. (2017) correspond to the maximum and minimum density values.

Figure 5 Comparison of centrifuge test results and finite element simulations (stages 1 & 2). (a) U1VD-A, H/D_h = 5.9; (b) U1MD, H/D_h = 4.5; (c) U1VD-B, H/D_h =7.4; (d) U2VD, $H/D_{h,1}$ =7.4 & $H/D_{h,2}$ = 5.4

900 Figure 6 Failure mechanism development at different anchor imposed displacements ($u_{y,imposed}$), single
901 helix in very dense sand (U1VD-B, H/D_h = 7.4), the dashed line indicates the failure mechanism
902 assumed by (Giampa et al. 2017).
903 Figure 7 Failure mechanism development at different anchor imposed displacements ($u_{y,imposed}$),
904 double helix in very dense sand (U2VD, H/D_h=7.4& 5.4), the inclined dashed line indicates the failure
905 mechanism assumed by (Giampa et al. 2017).
906 Figure 8 Comparison of the indicators of failure at the anchor's head ($u_{y,imposed}$), (U1VD-B) and soil-soil
907 interface, the dashed line indicates the soil-soil interface
908 Figure 9 Consideration of cross-section along the assumed failure mechanism for the single helix
909 embedded in very dense sand (U1VD-B), ξ is the distance from the edge of the plate in the direction
910 of the cross-section, τ_{max} is the maximum shear stress that could be mobilised (=$\sigma'_N \tan \phi' pk$).
911 Figure 10 Comparison of the stress distribution along a cross-section (inclined at ψ degrees to the
912 vertical) and along the interface elements for the single helix (U1VD-B), after a vertical displacement
913 $u_y = 0.3D_h$
914 Figure 11 Consideration of the cross-section along the assumed mechanism (ψ = 17°) for a single
915 helix screw anchor (D_h = 1.7m) embedded at different depths in very dense (VD) sand, stage 1
916 simulations, ξ is the distance from the edge of the plate in the direction of the cross-section, τ_{max} is
917 the maximum shear stress that could be mobilised (=$\sigma'_N \tan \phi' pk$).
918 Figure 12 Normalised distance along the failure plane over which the shear strain γ_s is larger or equal
919 to 10% with respect to normalised plate depth
920 Figure 13 Comparison of bearing factors N_γ for a single helix screw anchor (D_h = 1.7m) at two
921 different densities and stage 2 (enhanced capacity). (a) D_r = 57%; (b) D_r = 84%.
922 Figure 14 Comparison of unloading/reloading Young modulus E_{ur} (a-b) and effective average stress p'
923 (c-d) after a step-installation procedure (a, c) or after a single compression load (b, d). The inclined
924 dashed line indicates the soil-soil interface position in stage 2.

925 Figure 15 Idealisation of the installation effect on the soil behaviour, based on the small-strain
926 Hardening soil model. (a) Effect of previous shearing; (b) Effect of average stress increase.
927 Figure 16 Comparison of centrifuge (U1VD-A, H/D_h = 5.9) and numerical solutions with different
928 imposed failure mechanisms.
929
930

TABLE CAPTION LIST

Table 1 Geometry, crowd force (Fy,min) and uplift capacity (Fy) of the different screw pile models at prototype scale for UoD (Davidson et al. 2019) and UWA (Hao et al. 2018) tests

Table 2 Properties of the plate elements (identical for pile core and helices), assumed identical for all tests

Table 3 Number of elements and nodes of the meshes for each simulation (stage 1)

Table 4 HSsmall parameters for the HST95 Congleton sand, after (Al-Defae et al. 2013, Lauder et al. 2013, Al-Baghdadi et al. 2017a), reference stiffness is for a reference pressure p^{ref} = 100kPa.

Table 4 Comparison of the uplift capacity and CPU run time as a function of the mesh refinement for the U1VD-B. The CPU time is normalised with respect to the fastest simulation (mesh #1)

Table 6 Effect of the preloading level ($F_{y0,max}$) on the uplift capacity (F_y) of the single deep helix (U1VD-B,)

Table 7 Comparison of the pitch to helix diameter ratio for different studies

946 **TABLES**

947 Table 1 Geometry, crowd force (Fy,min) and uplift capacity (Fy) of the different screw pile models at
948 prototype scale for UoD (after Davidson et al. 2019) and UWA (after Hao et al. 2018) tests

	Helix number [-]	D_r [%]	D_h [m]	D_s [m]	H [m]	H/D_h	Pitch [m]	$F_{y,min}$ [MN]	F_y [MN]
UoD tests									
U1VD-A	1	84	1.7	0.88	10	5.9	0.56	-12.5	6.4
U1VD-B	1	84	1.7	0.88	12.5	7.4	0.56	-18.0	10.6
U2VD	2	84	1.7	0.88	9.1/12.5	5.4/7.4	0.56	-20.2	10.8
U1MD	1	57	3.4	1.13	15.2	4.5	0.56	-21.0	15
UWA tests									
SP3	1	85.8	0.4	0.094	1.2	3	0.1	Wished-in-Place	0.023
SP6	1	85.8	0.4	0.094	2.4	6	0.1		0.109
SP9	1	85.8	0.4	0.094	3.6	9	0.1		0.236
SP12-a	1	85.5	0.4	0.094	4.8	12	0.1		0.358
SP12-b	1	85.4	0.4	0.094	4.8	12	0.1		0.313
SH2	1	86.7	0.4	0.094	0.8	2	0.1		0.001
SH3-a	1	86.4	0.4	0.094	1.2	3	0.1		0.022
SH3-b	1	96.2	0.4	0.094	1.2	3	0.1		0.023
SH4	1	86.7	0.4	0.094	1.6	4	0.1		0.043
SH6-a	1	86.4	0.4	0.094	2.4	6	0.1		0.108
SH6-c	1	96.2	0.4	0.094	2.4	6	0.1		0.122
SH7.5	1	90.0	0.4	0.094	3.0	7.5	0.1		0.162
SH8-a	1	86.4	0.4	0.094	3.2	8	0.1		0.176
SH8-b	1	96.4	0.4	0.094	3.2	8	0.1		0.218
SH9-a	1	88.8	0.4	0.094	3.6	9	0.1		0.250
SH9-b	1	96.1	0.4	0.094	3.6	9	0.1		0.270
SH9-c	1	96.2	0.4	0.094	3.6	9	0.1		0.260
SH10	1	96.4	0.4	0.094	4.0	10	0.1		0.310
SH10.5	1	90.0	0.4	0.094	4.0	10.5	0.1		0.272
SH12-a	1	85.4	0.4	0.094	4.8	12	0.1		0.322
SH12-b		91.7	0.4	0.094	4.8	12	0.1		0.365

949

950

951 Table 2 Properties of the plate elements (identical for pile core and helices), assumed identical for all
952 tests

EA [GN/m]	EI [MNm²/m]	t_{equiv} [m]	ν [-]
38.08	39.8	0.112	0.3

953

954

955

956

957

958

Table 3 Number of elements and nodes of the meshes for each simulation (stage 1). The minimum element size was normalised with respect to the helix diameter D_h.

		Elements	Min El. Size/D_h [-]	Nodes
UoD	U1VD-A	2534	0.03	21206
	U1VD-B	3175	0.04	26476
	U2VD	3779	0.03	31428
	U1MD	3674	0.03	30296
UWA	SH2	3888	0.05	31770
	SH4	3514	0.05	28918
	SH6	4517	0.05	37128
	SH7.5	6382	0.05	52002
	SH9	5187	0.05	42448

963

964 Table 4 HSsmall parameters for the HST95 Congleton sand, after **(after Lauder et al. 2013; Al-Defae**
965 **et al. 2013; Al-Baghdadi et al. 2017a)**, reference stiffness is for a reference pressure p^{ref} = 100kPa.

Soil parameters		Unit	Equation	D_r = 57%	D_r = 84%
Min. void ratio	e_{min}	[-]		0.469	0.469
Max. void ratio	e_{max}	[-]		0.769	0.769
Initial void ratio	e_0	[-]		0.597	0.515
Peak friction angle	ϕ'_{pk}	[°]	$20\,I_D$+29	40.4	45.8
Dilatancy angle	ψ	[°]	$25\,I_D-4$	10.25	17
Effective apparent cohesion	c′	[kPa]	$25\,I_D$+20.22	1.0	1.0
Oedometer stiffness	E_{oed}^{ref}	[MPa]	$25\,I_D$+20.22	34.5	41.2
Secant stiffness	E_{50}^{ref}	[MPa]	$1.25\,E_{oed}^{ref}$	43.1	51.5
Unloading/reloading stiffness	E_{ur}^{ref}	[MPa]	$3\,E_{oed}^{ref}$	103.4	123.7
Material parameter	M	[-]	$0.6-0.1\,I_D$	0.54	0.52
Unloading/reloading Poisson's ratio	ν_{ur}	[-]		0.2	0.2
Reference shear strain	$\gamma_{0.7}$	[-]	$\left(1.7\,I_D+0.67\right)\cdot 10$	$1.64\cdot10^{-4}$	$2.09\cdot10^{-4}$
Low strain shear modulus	G_0^{ref}	[MPa]	$50\,I_D$+88.8	118.8	130.8
Total unit weight	γ_{tot}	[kN/m³]	$30\,I_D$+14.5	19.83	20.30

966

967

Table 5 Comparison of the uplift capacity and CPU run time as a function of the mesh refinement for the U1VD-B (stage 1 simulation). The CPU time is normalised with respect to the fastest simulation (mesh #1). The average, maximum and minimum element sizes were normalised with respect to the helix diameter. The computer used had the following specifications: Intel® Xeon® CPU E5-1650 v4 @3.60GHz, 24GB RAM, 64-bit operating system.

Mesh		1	2	3	4	5
Elements	[-]	498	808	2175	3175	5678
Average El. size/D_h	[-]	0.94	0.73	0.37	0.29	0.22
Max El. Size/D_h	[-]	3.75	2.75	2.08	2.61	1.91
Min El. Size/ D_h	[-]	0.15	0.11	0.04	0.04	0.03
Nodes	[-]	4337	6878	18292	26746	46866
$F_{y,0.1\,D_h}$	[MN]	13.78	12.95	13.64	13.35	13.13
$F_{y,max}$	[MN]	14	14.83	14.58	15.09	15.23
Normalised CPU time	[s]	1	3.4	19.2	24.4	46.7

975 Table 6 Effect of the preloading level ($F_{y0,max}$) on the uplift capacity (F_y) of the single deep helix (U1VD-
976 B)

$F_{y0,max}$ [MN]	F_y [MN]
-9	10.9
-18	11.3
-27	12.1

977

978

FIGURES

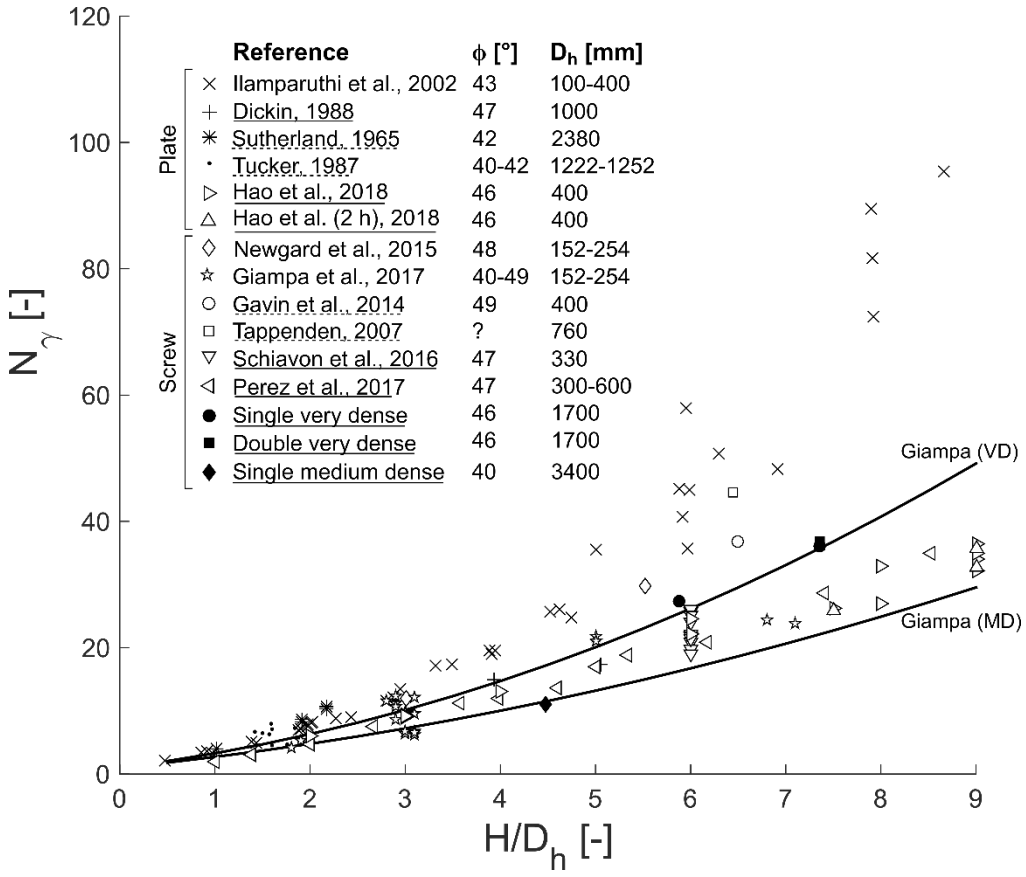

Figure 1 Comparison of centrifuge tests with respect to relatively large scale 1g, centrifuge and field experimental results, for plate anchors (wished in place, open markers) and screw anchors (installation effect, closed markers). Centrifuge and field tests are underlined by solid and dashed lines respectively. Single and double refer to the number of helices. The Giampa et al. (2017) criterion is calculated for very dense (VD) and medium-dense (MD) soil properties.

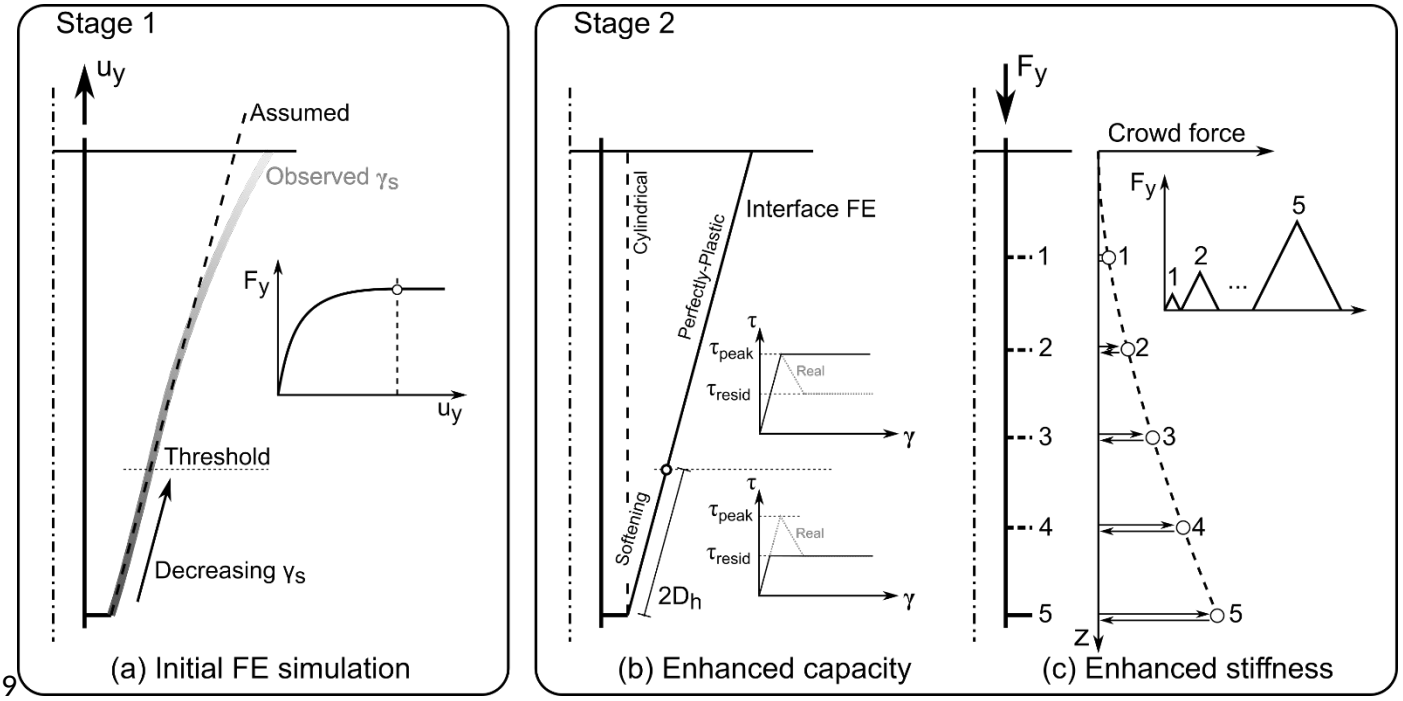

989

990 Figure 2 Schematic description of the multi-stage methodology

991

992

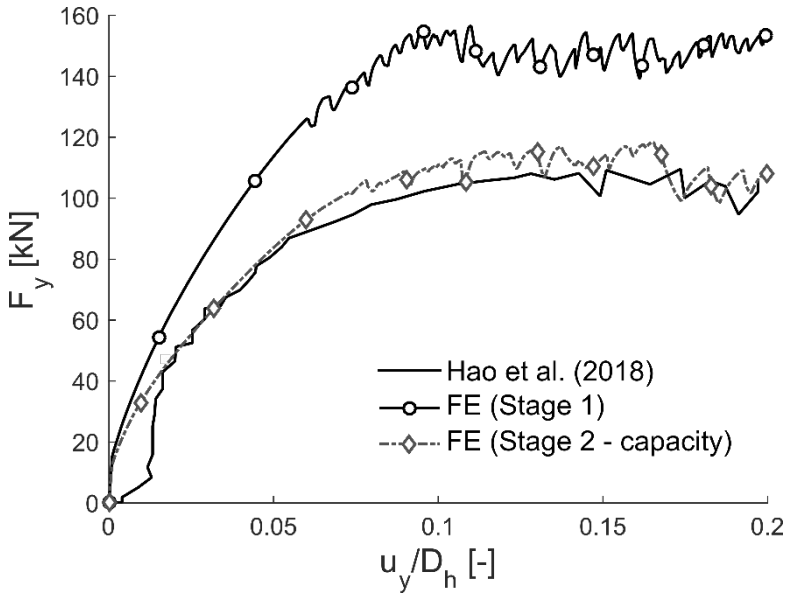

993

994 Figure 3 Comparison of the load-displacement relationship for the wished in place centrifuge tests
995 ($H/D_h = 6$) in dense sand from Hao et al. (2018) and numerical simulations (Stage 1 & Stage 2 –
996 capacity)

997

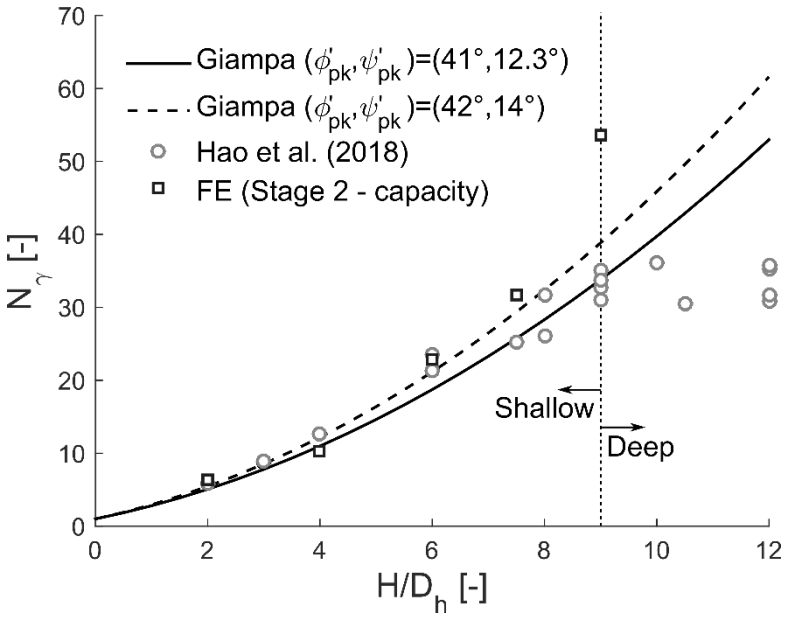

998

999 Figure 4 Comparison of wished in place centrifuge tests in dense sand from Hao et al. (2018) and
1000 numerical simulations (Stage 2 – capacity). The two sets of parameters used to calculate the
1001 analytical criterion of Giampa et al. (2017) correspond to the maximum and minimum density values.

1002

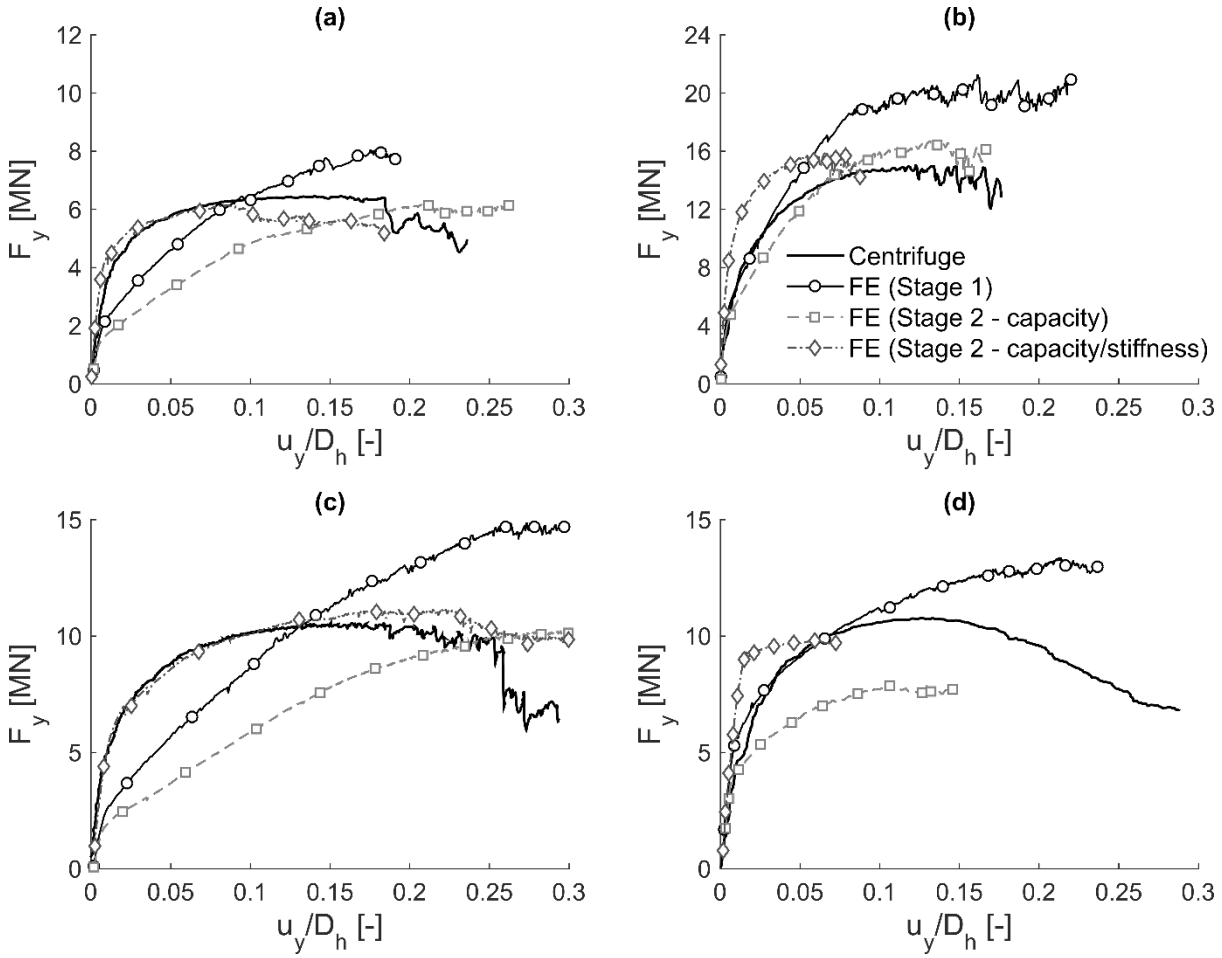

Figure 5 Comparison of centrifuge test results and finite element simulations (stages 1 & 2). (a) U1VD-A, H/D_h = 5.9; (b) U1MD, H/D_h = 4.5; (c) U1VD-B, H/D_h =7.4; (d) U2VD, $H/D_{h,1}$ =7.4 & $H/D_{h,2}$ = 5.4

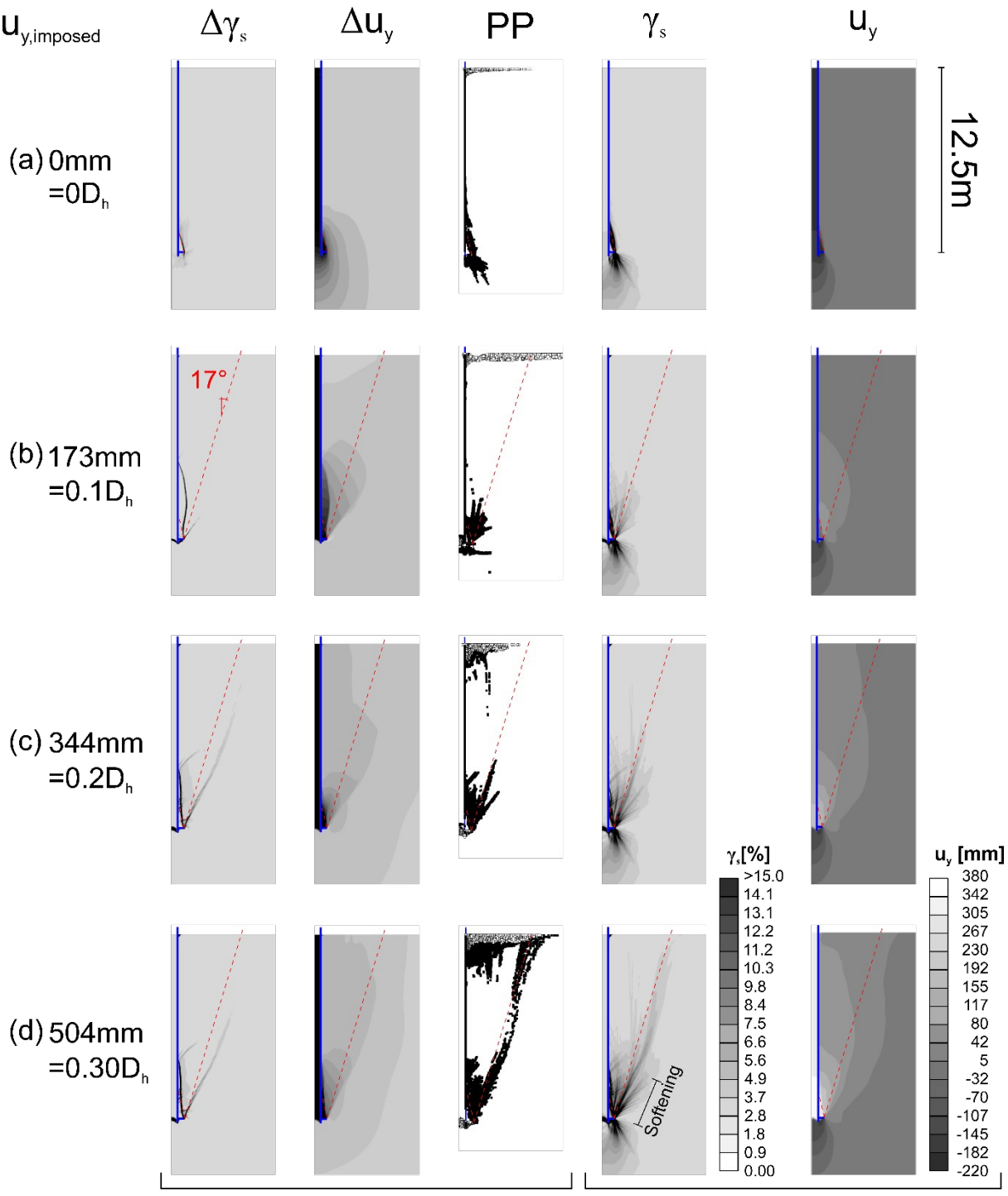

Figure 6 Failure mechanism development at different anchor imposed displacements ($u_{y,imposed}$), single helix in very dense sand (U1VD-B, H/D_h = 7.4), the dashed line indicates the failure mechanism assumed by Giampa et al. (2017).

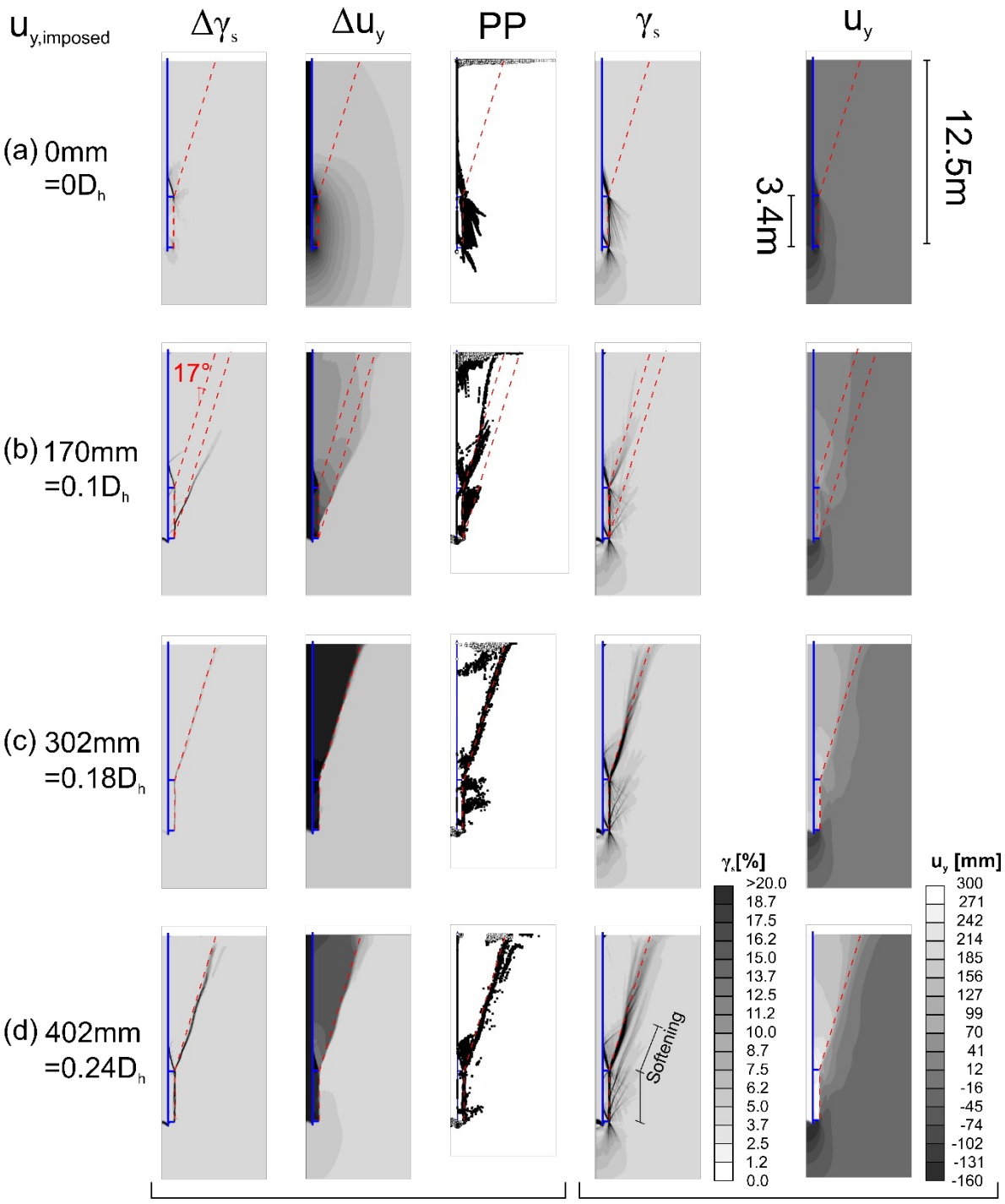

Figure 7 Failure mechanism development at different anchor imposed displacements ($u_{y,imposed}$), double helix in very dense sand (U2VD, H/D_h=7.4& 5.4), the inclined dashed line indicates the failure mechanism assumed by Giampa et al. (2017).

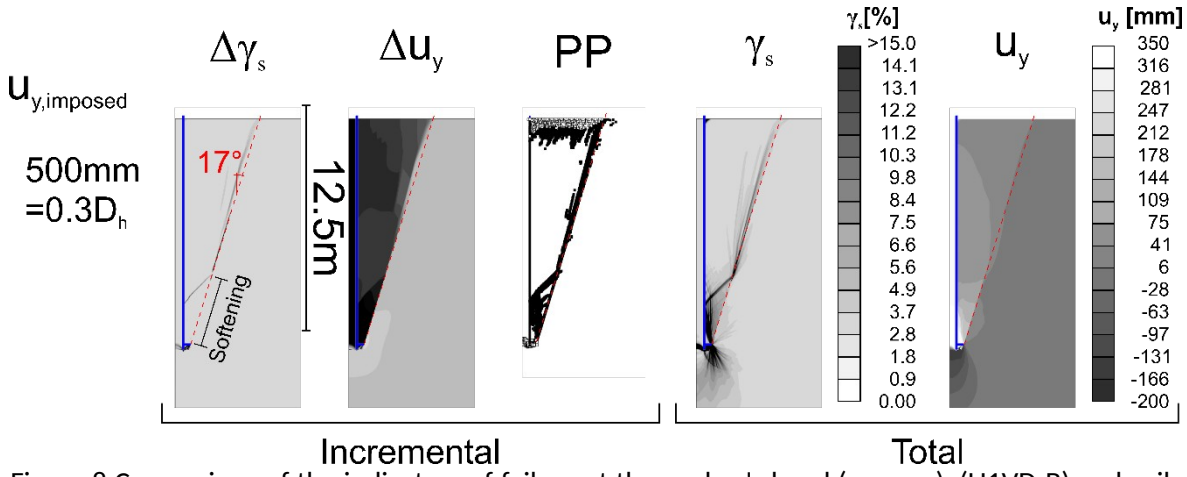

Figure 8 Comparison of the indicators of failure at the anchor's head ($u_{y,imposed}$), (U1VD-B) and soil-soil interface, the dashed line indicates the soil-soil interface

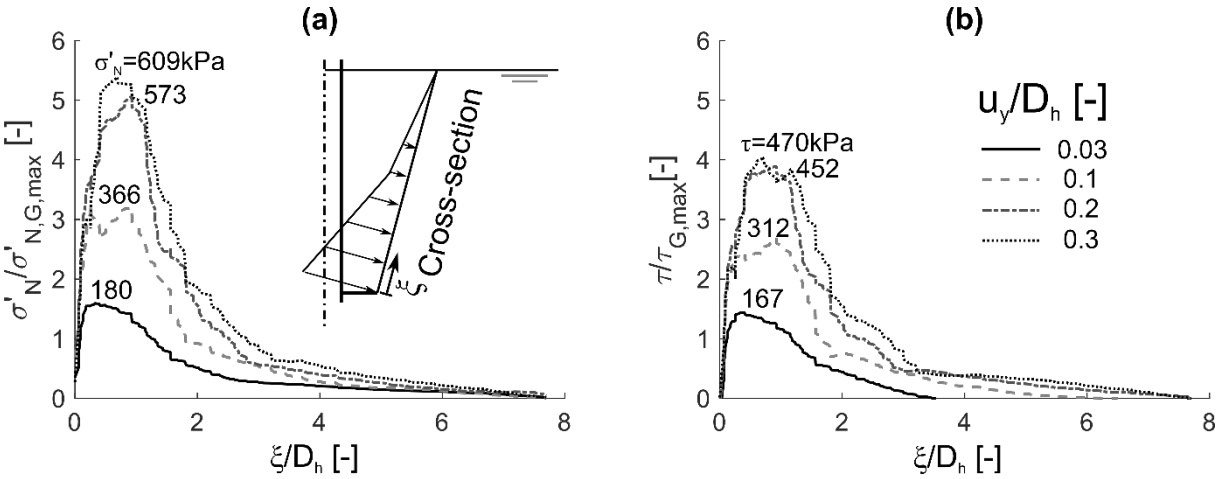

Figure 9 Consideration of cross-section along the assumed failure mechanism for the single helix embedded in very dense sand (U1VD-B), ξ is the distance from the edge of the plate in the direction of the cross-section, τ_{max} is the maximum shear stress that could be mobilised (=$\sigma'_N \tan \phi'_{pk}$).

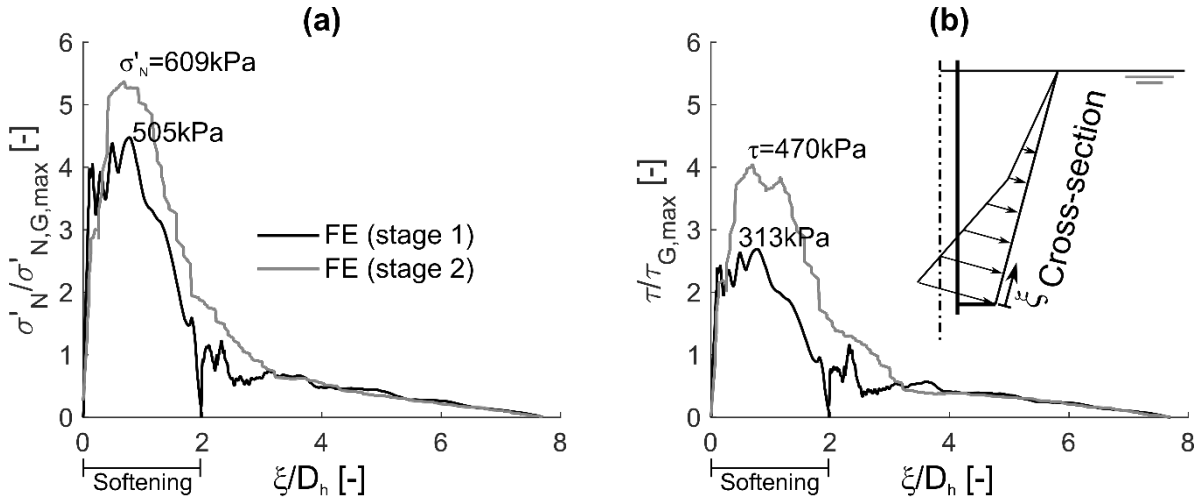

1030

1031 Figure 10 Comparison of the stress distribution along a cross-section (inclined at ψ degrees to the
1032 vertical) and along the interface elements for the single helix (U1VD-B), after a vertical displacement
1033 $u_y = 0.3D_h$

1034

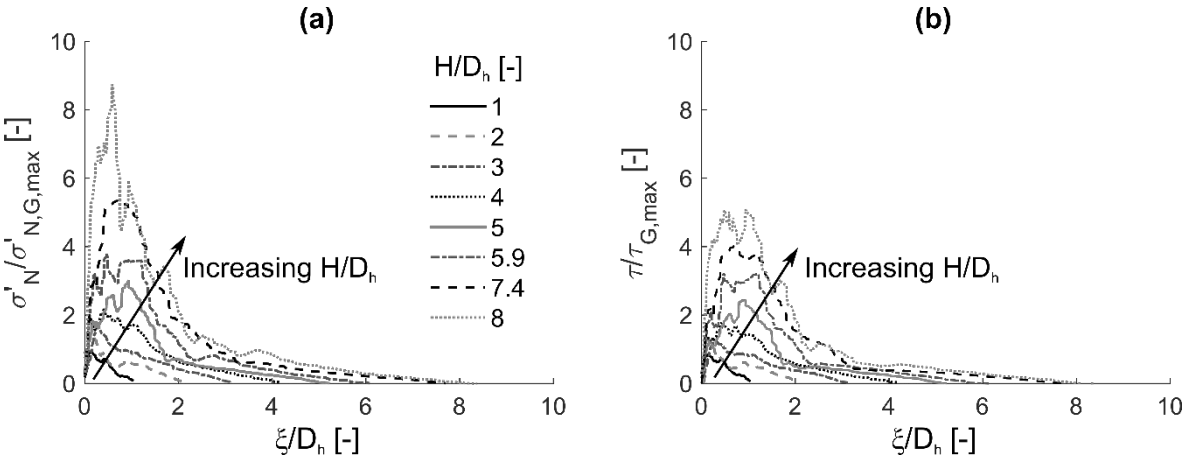

Figure 11 Consideration of the cross-section along the assumed mechanism (ψ = 17°) for a single helix screw anchor (D_h = 1.7m) embedded at different depths in very dense (VD) sand, stage 1 simulations, ξ is the distance from the edge of the plate in the direction of the cross-section, τ_{max} is the maximum shear stress that could be mobilised (=$\sigma'_N \tan \phi'_{pk}$).

1042

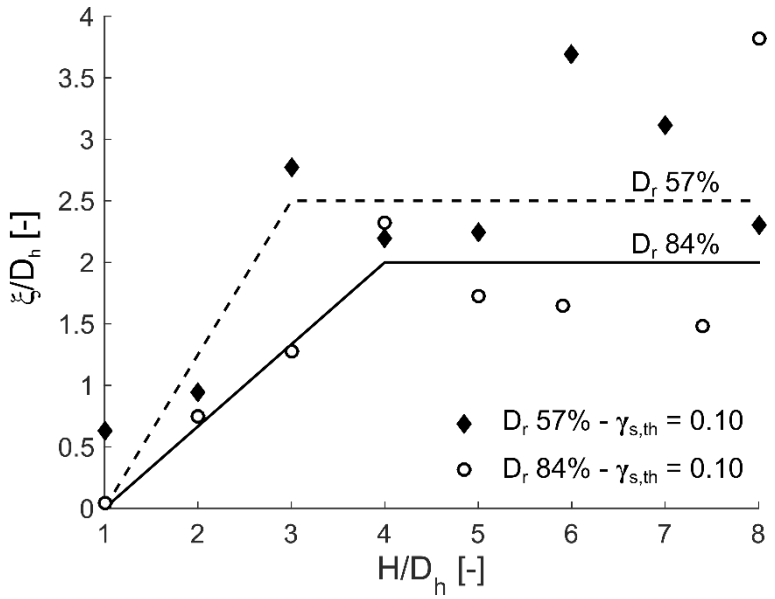

1043
1044 Figure 12 Normalised distance along the failure plane over which the shear strain γ_s is larger or equal
1045 to 10% with respect to normalised plate depth

1046

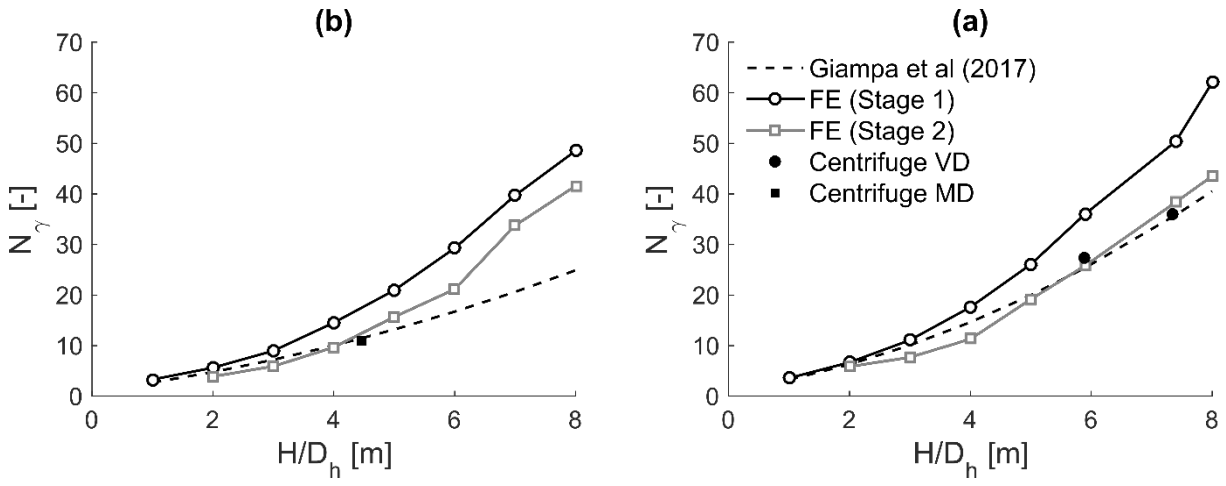

Figure 13 Comparison of bearing factors N_γ for a single helix screw anchor (D_h = 1.7m) at two different densities and stage 2 (enhanced capacity). (a) D_r = 57%; (b) D_r = 84%.

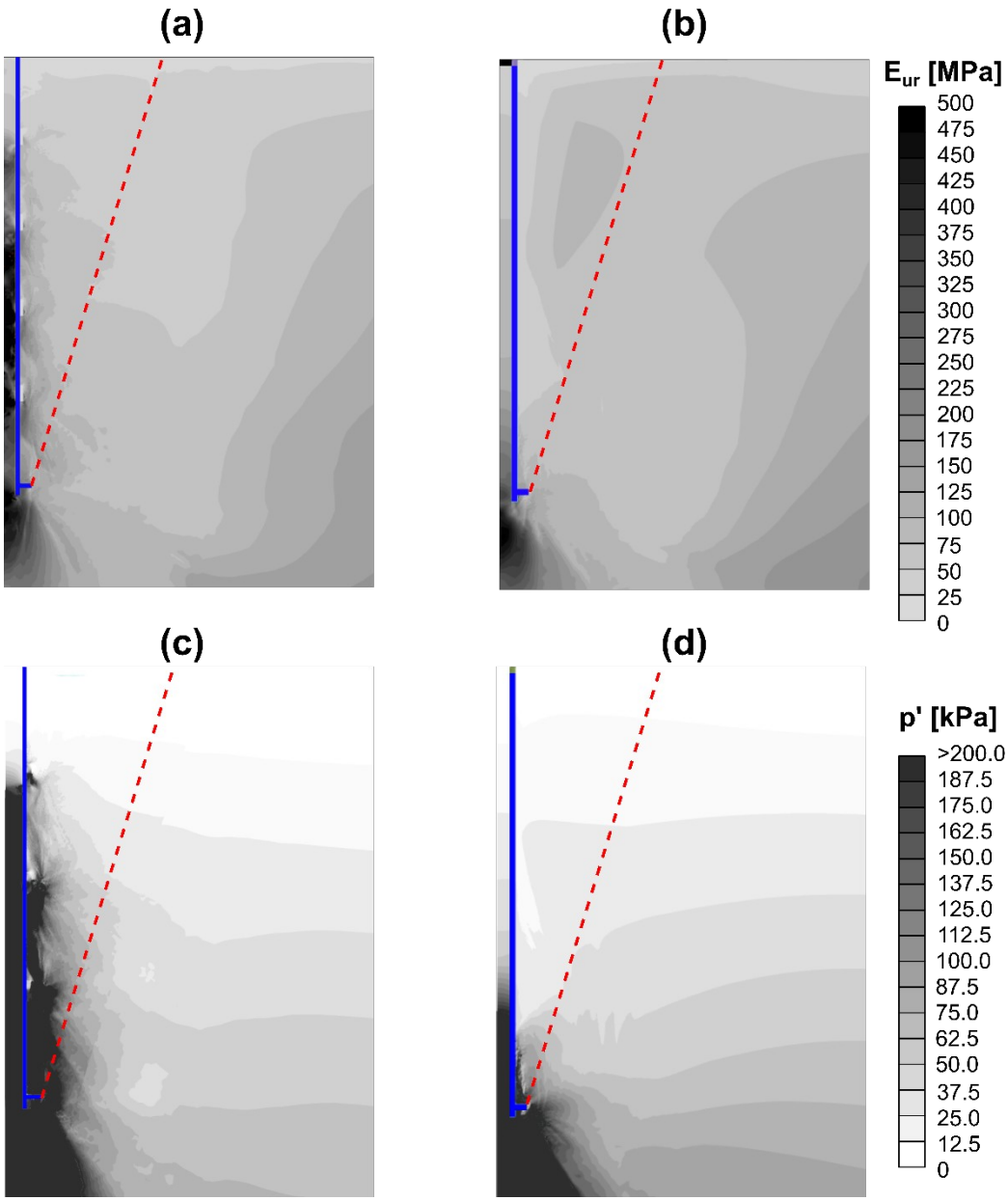

Figure 14 Comparison of unloading/reloading Young modulus E_{ur} (a-b) and effective average stress p' (c-d) after a step-installation procedure (a, c) or after a single compression load (b, d). The inclined dashed line indicates the soil-soil interface position in stage 2.

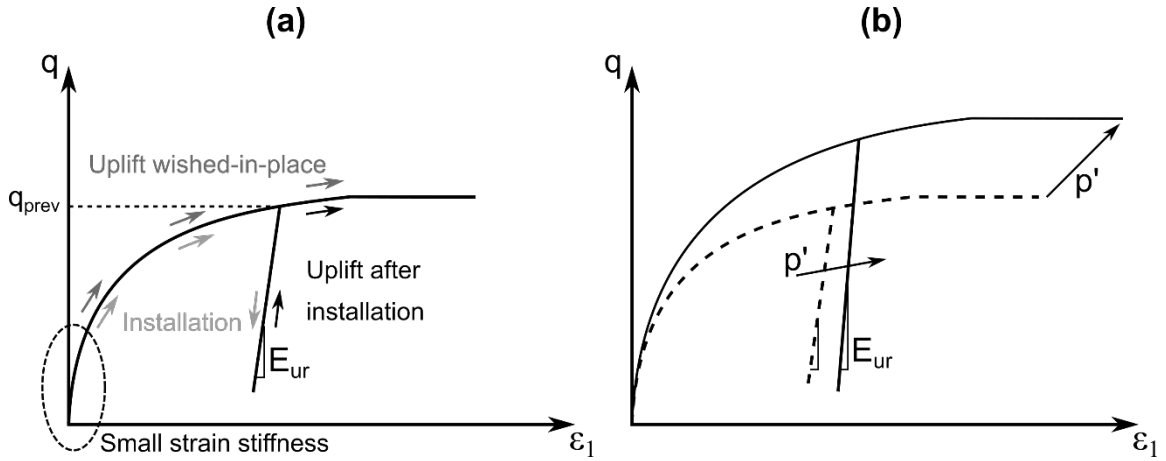

Figure 15 Idealisation of the installation effect on the soil behaviour, based on the small-strain Hardening soil model. (a) Effect of previous shearing; (b) Effect of average stress increase.

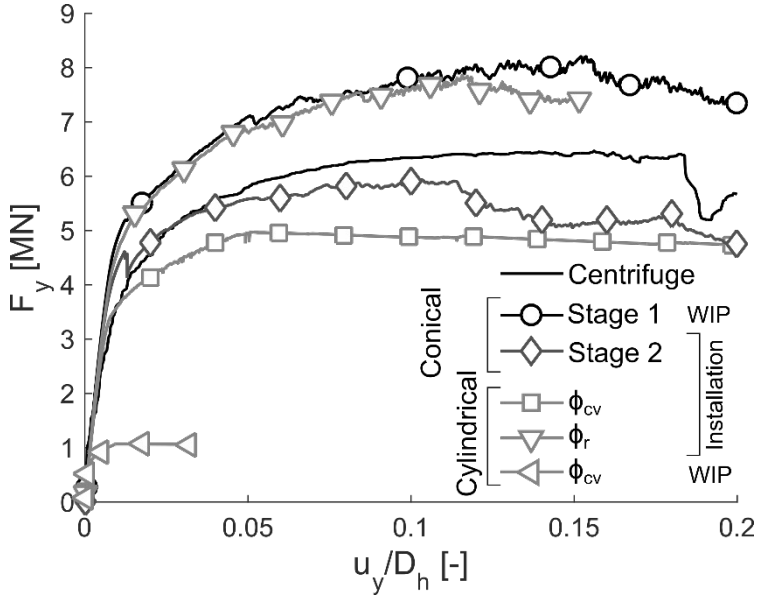

Figure 16 Comparison of centrifuge (U1VD-A, H/D_h = 5.9) and numerical solutions with different imposed failure mechanisms. Simulations include the installation process (Installation) or are wished-in-place (WIP)